Polarimetry for planetary atmospheres

What kind of diagnostic can we infer from polarimetric measurements?

Blue sky polarisation: Rayleigh diffusion

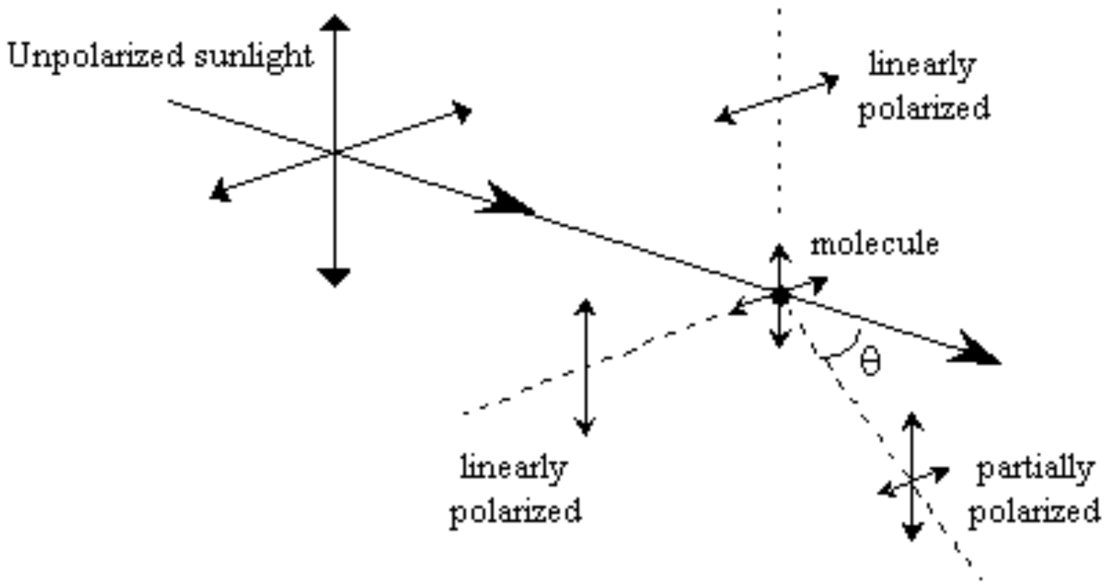

Polarisation by Rayleigh diffusion: very efficient since light is totally polarised when Θ=90°.

$$I_{Ray}(\cos\Theta) = \frac{3}{4}\left(1 + \cos^2(\Theta)\right).$$

$$P = \frac{1 - \cos^2\Theta}{1 + \cos^2\Theta}.$$

Multiple scattering

- Generally randomize the polarisation direction
- Lower the observable polarisation
- But create particular features which does not exist with single scattering
- Often really important to take into account but almost complicated
    - Need generally for MC simulation
    - Need for full 3D codes. Geometrical simplification are very difficult.
        - Useful when the secondary or more scattering are of the same order of magnitude

Example of the twilight sky (Ugolnikov 2004)

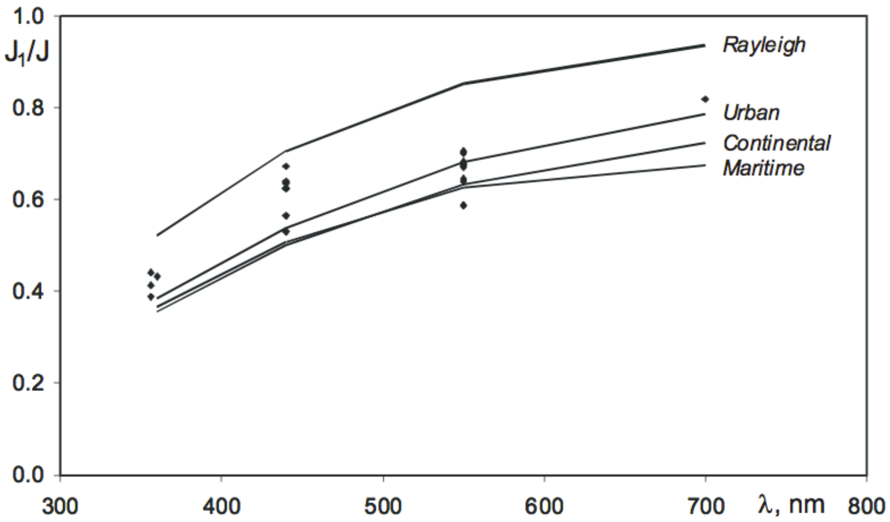

Figure 2. The contribution of single scattering in the twilight sky background at the zenith at the moment of sunrise (sunset) obtained by the observational method (dots) and radiation transfer simulation (lines).

(a)

Kind of particle	Dust	Water-soluble	Oceanic	Soot
Function of size distribution	lognormal	lognormal	lognormal	lognormal
Parameters	0.5 mkm, 2.99	0.005 mkm, 2.99	0.3 mkm, 2.51	0.0118 mkm, 2.00

(b)

Kind of aerosol	Dust	Water-soluble	Oceanic	Soot
Urban	17%	61%	0%	22%
Continental	70%	29%	0%	1%
Maritime	0%	5%	95%	0%

Table 1. Kinds of aerosol particles (a) and percentage of aerosol particles in different kinds of aerosol (b) defined in [9].

Polarisation pattern in the real sky

The theoretical patterns of the degree and angle of polarization of skylight were calculated using the single-scattering Rayleigh model (Coulson, 1988). In the single-scattering Rayleigh atmosphere, the degree of linear polarization of skylight δ is expressed in Equation 1 and Equation 2 as:

$$\delta = \delta_{max} \sin^2\gamma / (1 + \cos^2\gamma) , \qquad (1)$$

$$\cos\gamma = \sin\theta_s \sin\theta \cos\psi + \cos\theta_s \cos\theta , \qquad (2)$$

where γ is the angular distance between the observed celestial point and the sun, θ_s is the solar zenith angle and θ and ψ are the angular distances of the observed point from the zenith and the solar meridian, respectively. For a given θ_s, δ_{max} was determined from the patterns of the degree of polarization of skylight measured by full-sky imaging polarimetry. In the single-scattering Rayleigh atmosphere, the direction (or angle) of polarization is perpendicular to the plane of scattering determined by the observer, the celestial point observed and the sun. In the single-scattering Rayleigh model, the polarization of skylight is independent of the wavelength.

2936 I. POMOZI, G. HORVÁTH AND R. WEHNER

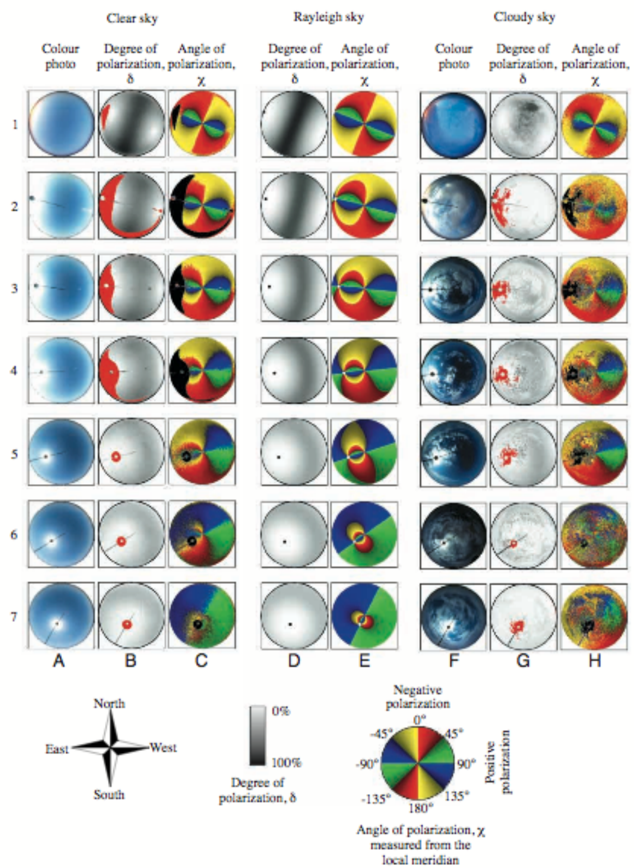

Neutral points: important for animal navigation.

There are three commonly detectable points of zero polarization of diffuse sky radiation (known as neutral points) lying along the vertical circle through the sun.

- The Arago point, named after its discoverer, is customarily located at about 20° above the antisolar point; but it lies at higher altitudes in turbid air. The latter property makes the Arago distance a useful measure of atmospheric turbidity.
- The Babinet point, discovered by Babinet in 1840, is located about 15° to 20° above the sun, hence it is difficult to observe because of solar glare.
- The Brewster point, discovered by Brewster in 1840, is located about 15° to 20° below the sun; hence it is difficult to observe because of solar glare.

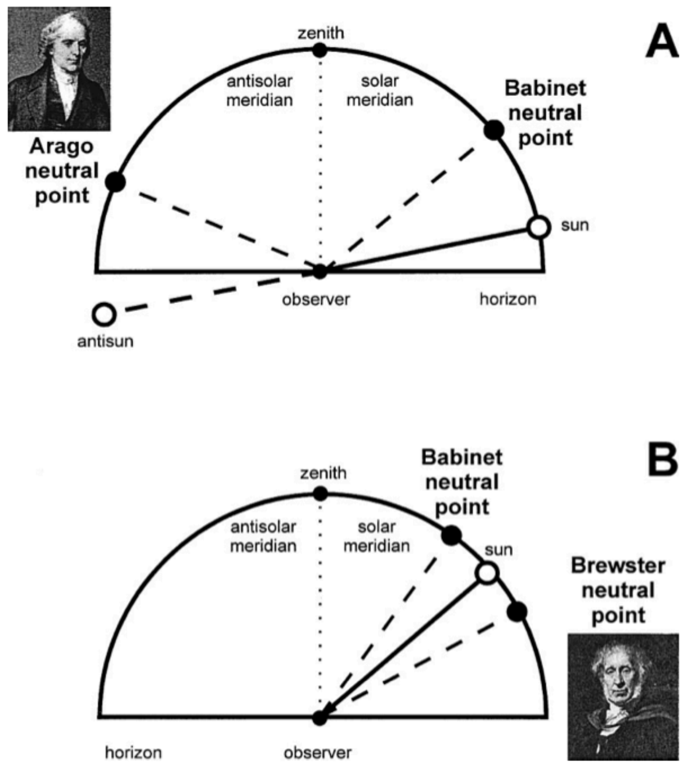

Fig. 1A,B. Schematic diagram showing the normal positions of the Arago, Babinet, and Brewster neutral points of skylight polarization in the plane of the sun's vertical. *Insets*, the portraits of Dominique Francois Jean Arago (1786–1853) and Sir David Brewster (1781–1868), the discoverer of the first and third neutral points, respectively

Horvath et al. 1998, 2002.

According to theoretical considerations and computer simulations, there should exist an additional neutral point approximately opposite to the Babinet point, which can be observed only at higher altitudes in the air or space:

First observation of the fourth neutral polarization point in the atmosphere

Horvath et al. 2002.

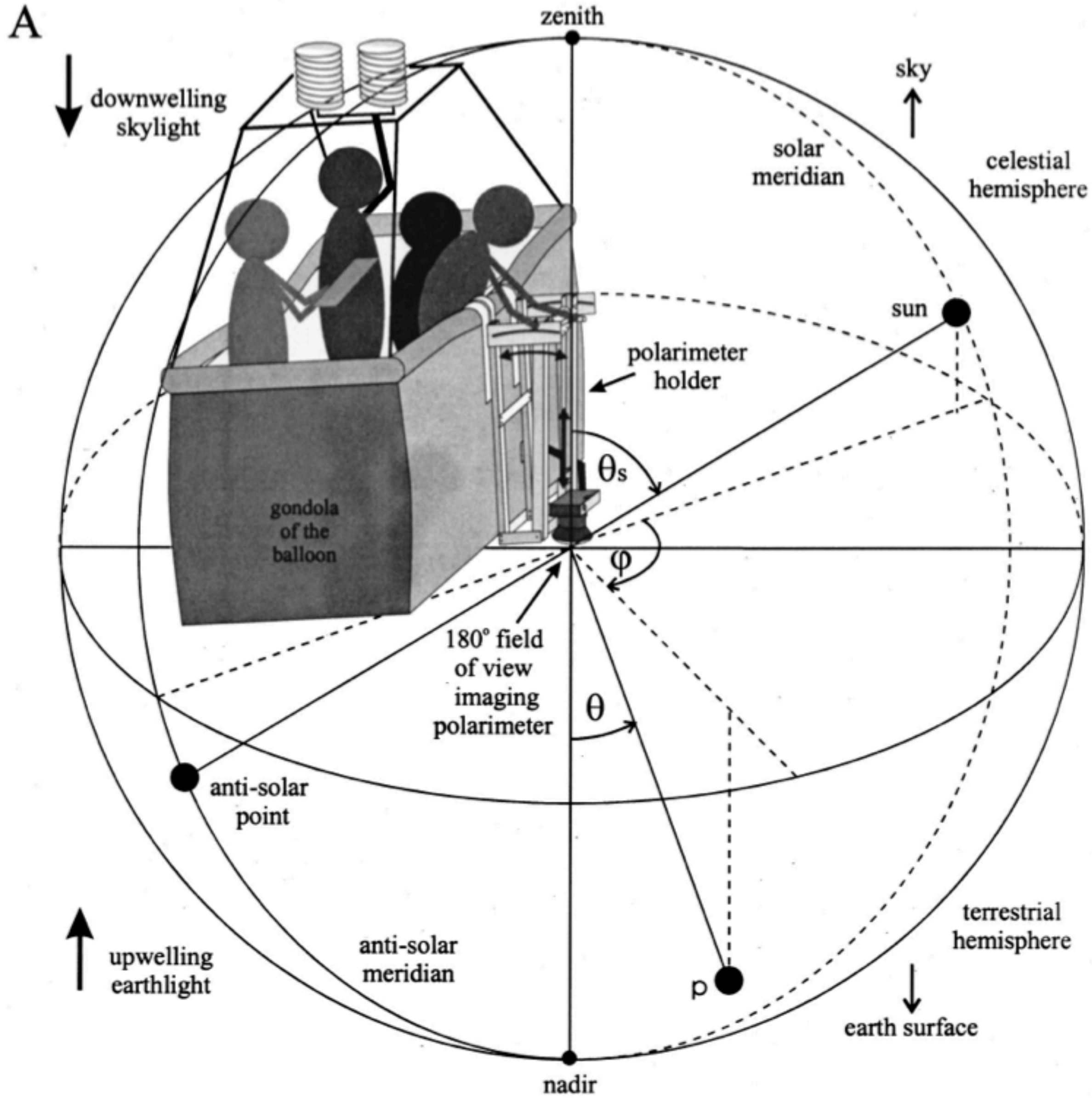

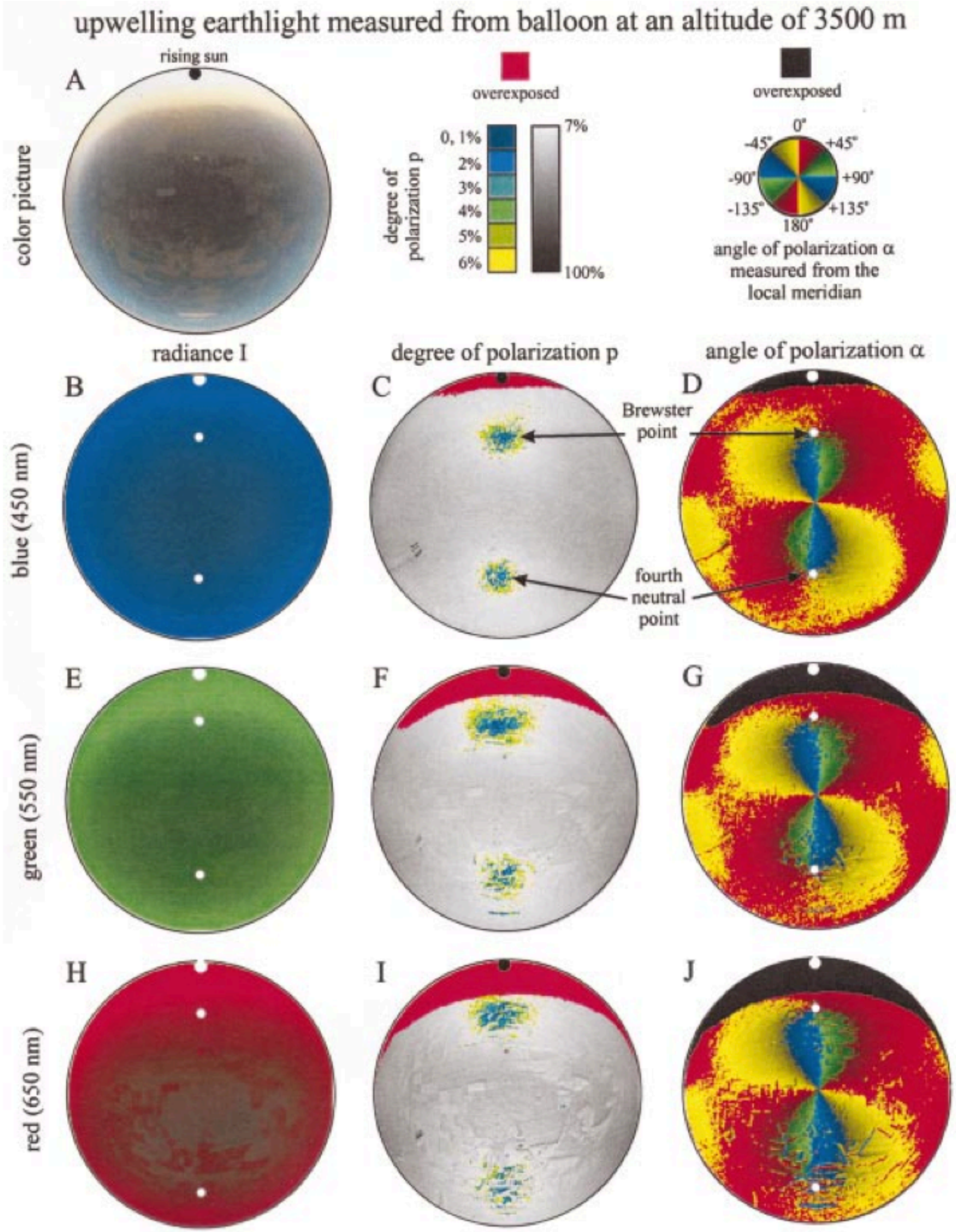

Horvath et al. 2002

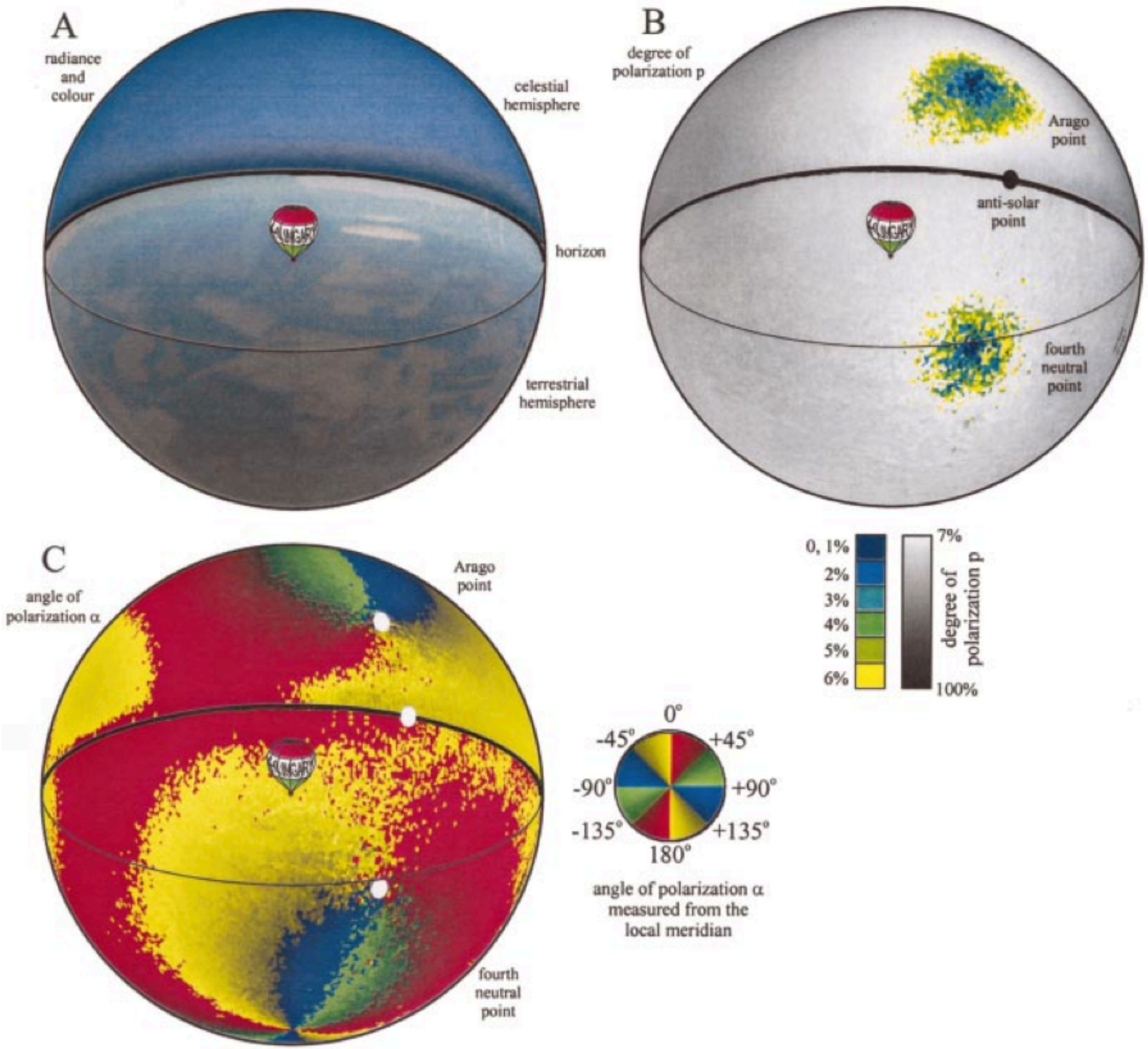

Fig. 8. Three-dimensional spatial distribution of radiance and color (A), degree (B), and angle (C) of linear polarization as well as the Arago and fourth neutral points observable around a hot air balloon at 450 nm and at an altitude of 3500 m. Each sphere in the picture is the combination of the patterns of parts A, C, D in Figs. 4 and 5.

Cloudy sky

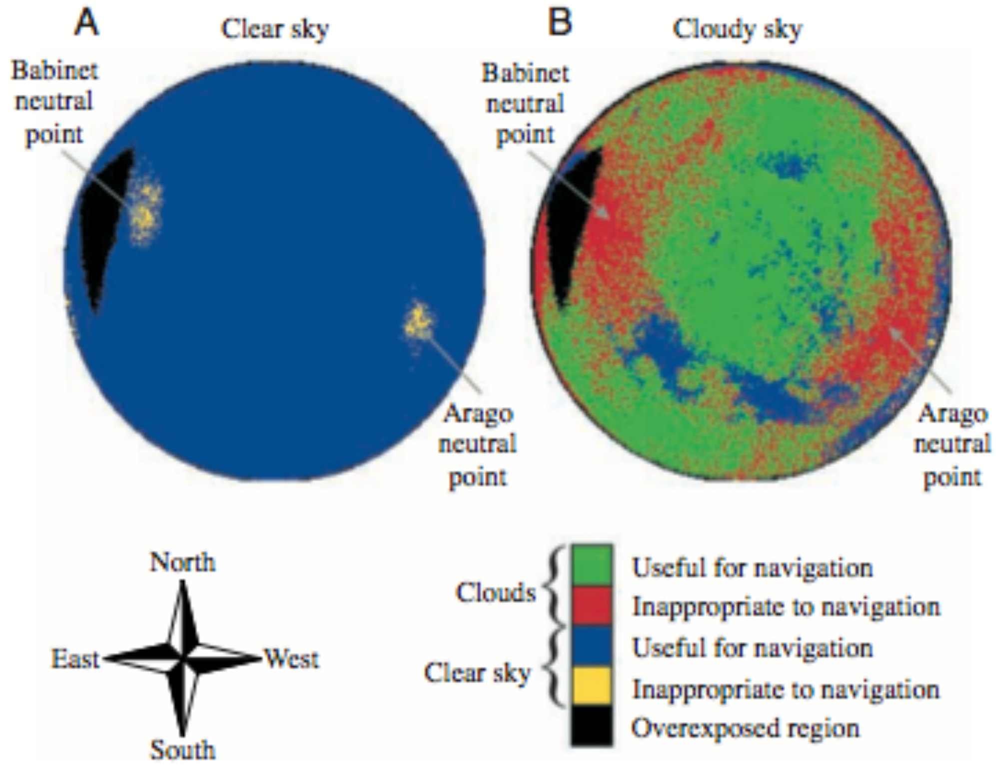

Fig. 3. Regions of the clear (A) and cloudy (B) sky shown in Fig. 1A,1 and F,1, respectively, with polarization patterns useful for or inappropriate to reliable cricket navigation calculated on the basis of the celestial polarization patterns measured by full-sky imaging polarimetry in the blue (450 nm) spectral range. Blue (useful for navigation): regions of the clear sky where the degree of polarization $\delta > 5\%$. Yellow (inappropriate to navigation): regions of the clear sky where $\delta \leq 5\%$. Green (useful for navigation): regions of the clouds where $\delta > 5\%$ and $|\chi_{clear\ sky} - \chi_{clouds}| \leq 6.5°$, where χ is the angle of polarization. Red (inappropriate to navigation): regions of the clouds where $\delta \leq 5\%$ and/or $|\chi_{clear\ sky} - \chi_{clouds}| > 6.5°$. Black: region of the sky where the photoemulsion was overexposed. The numerical values of δ, $\chi_{clear\ sky}$ and χ_{clouds} originate from quantitative full-sky measurements.

Twilight sky

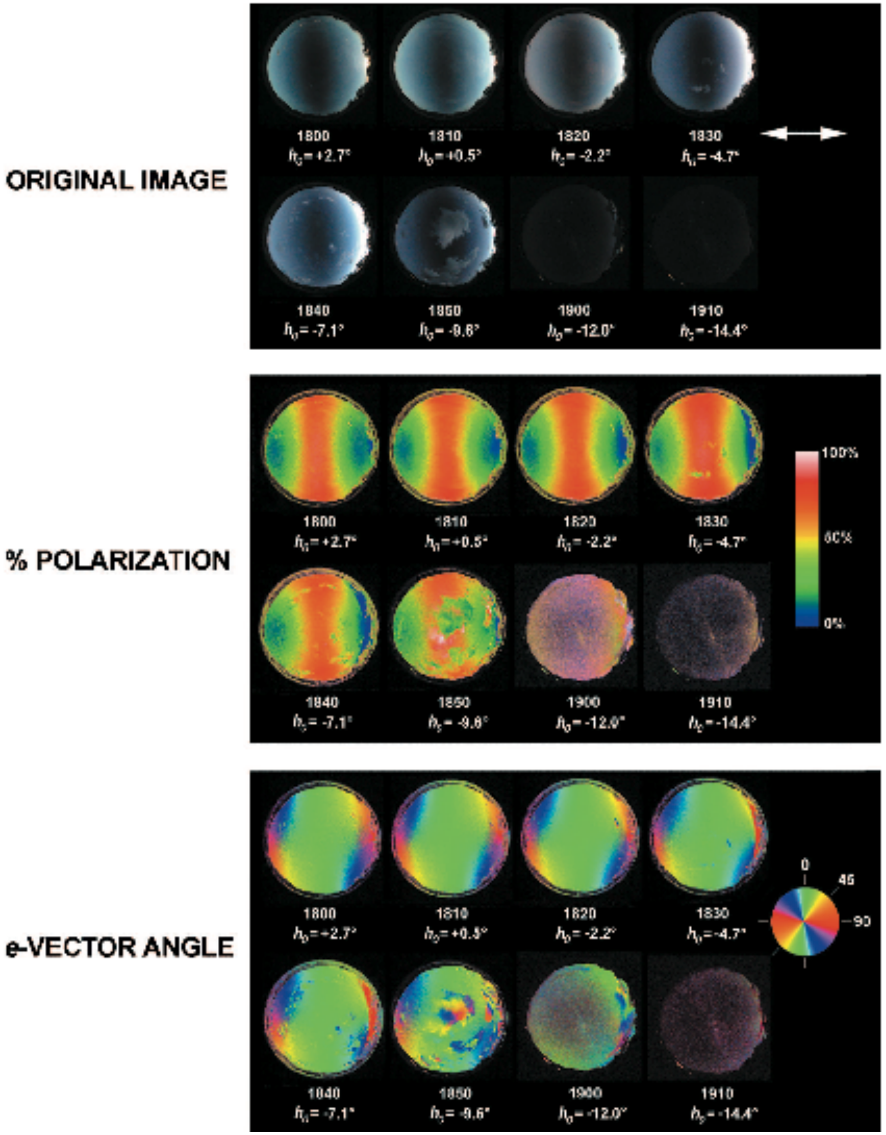

In fact polarisation pattern can be seen up sza=108°
Pattern and direction typical of multiple scattering phenomena.

Fig. 1. Linear polarization of the sky at sunset and during evening twilight. Full-sky images were acquired using a Nikon Coolpix 5700 digital camera with a fisheye lens attachment having a linear polarizing filter mounted between the lens and the camera itself, and polarization series of images were acquired as described in the text. Spectrally integrated data were acquired on 15 September 2004 at Lizard Island, Australia (sunset, 1814; limit of astronomical twilight, 1925; local time is Universal Time + 10 h). Each image is labeled with the local time at which data were acquired as well as the solar elevation, h_0. In all panels, the zenith is in the center, N is to the top, and E to the left. The top set of images are original digital photographs acquired when the polarizing filter was oriented E–W (indicated by the double-headed arrow), emphasizing the dark band of N–S e-vector orientation. The middle set shows analyzed % polarization (P_L) in false color, encoded as displayed in the key to the right. The bottom set indicates e-vector angle, also in false color as coded in the key to the right. The odd color patterns seen in some of the images depicting % polarization or e-vector angle are caused by clouds moving between images in original sets of exposures.

Polarisation by aerosols

- General principles
  - Dust
  - Ice cloud
  - Liquid water cloud
    - Various possible scattering particles from molecules to large dust or droplets
    - Need for accurate study of the phase fucntion and angular polarisation pattern.
    - A powerfull diagnostic tool of atmospheric
      - » But strongly difficult in case of multiple scattering situation

- For phase function and polarisation of particular particles: see Alexander A. Kokhanovsky (Editor); Light Scattering. Reviews of Single and Multiple Light Scattering

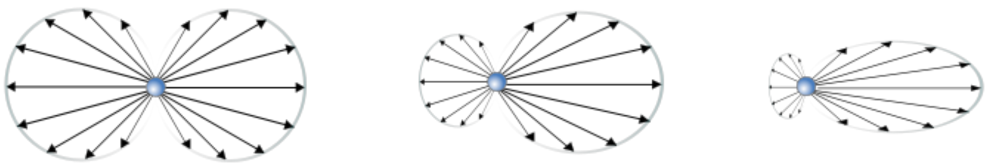

http://omlc.ogi.edu/calc/mie_calc.html

Twilight sky (Ugolnikov 2004)

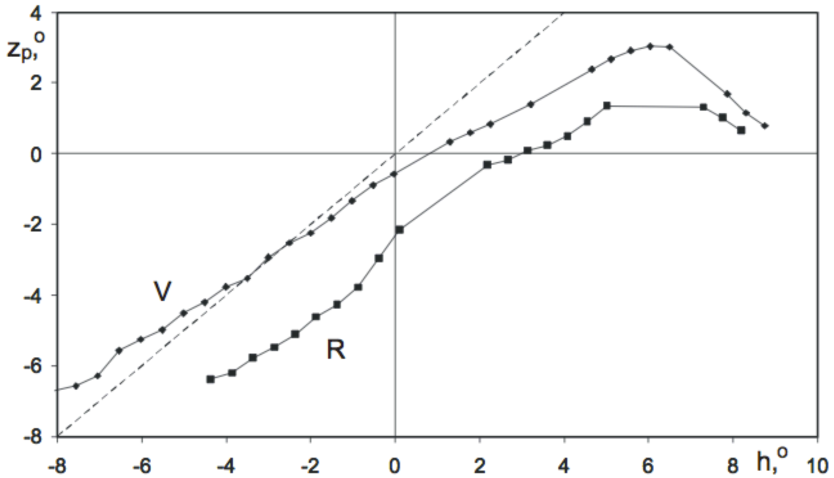

Figure 1. The motion of the maximum polarization point with the Sun depression in the evening of 06.08.2000 in V and R color bands (the dashed line corresponds to the case of pure Rayleigh single scattering).

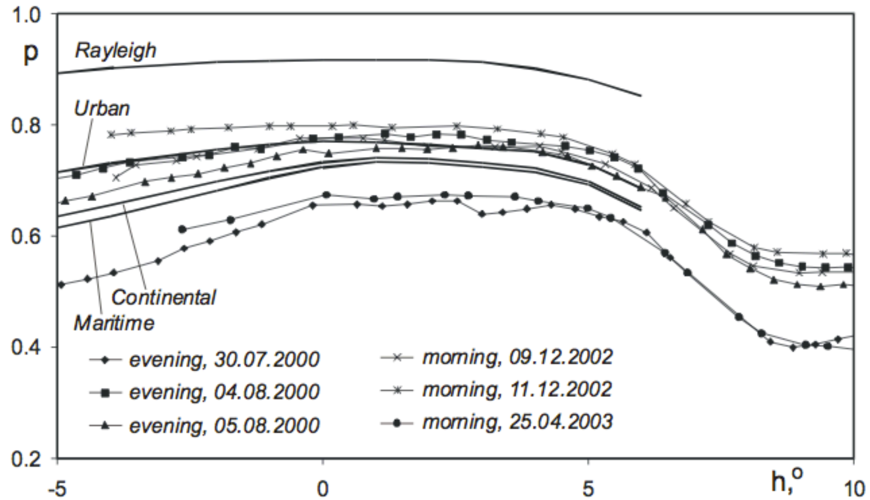

Figure 3. The dependencies of the sky polarization at the zenith on the Sun depression under horizon for different observation dates in V band (550 nm) compared with the results of numerical simulation of radiation transfer (bold lines).

Polarisation from other planets atmospheres

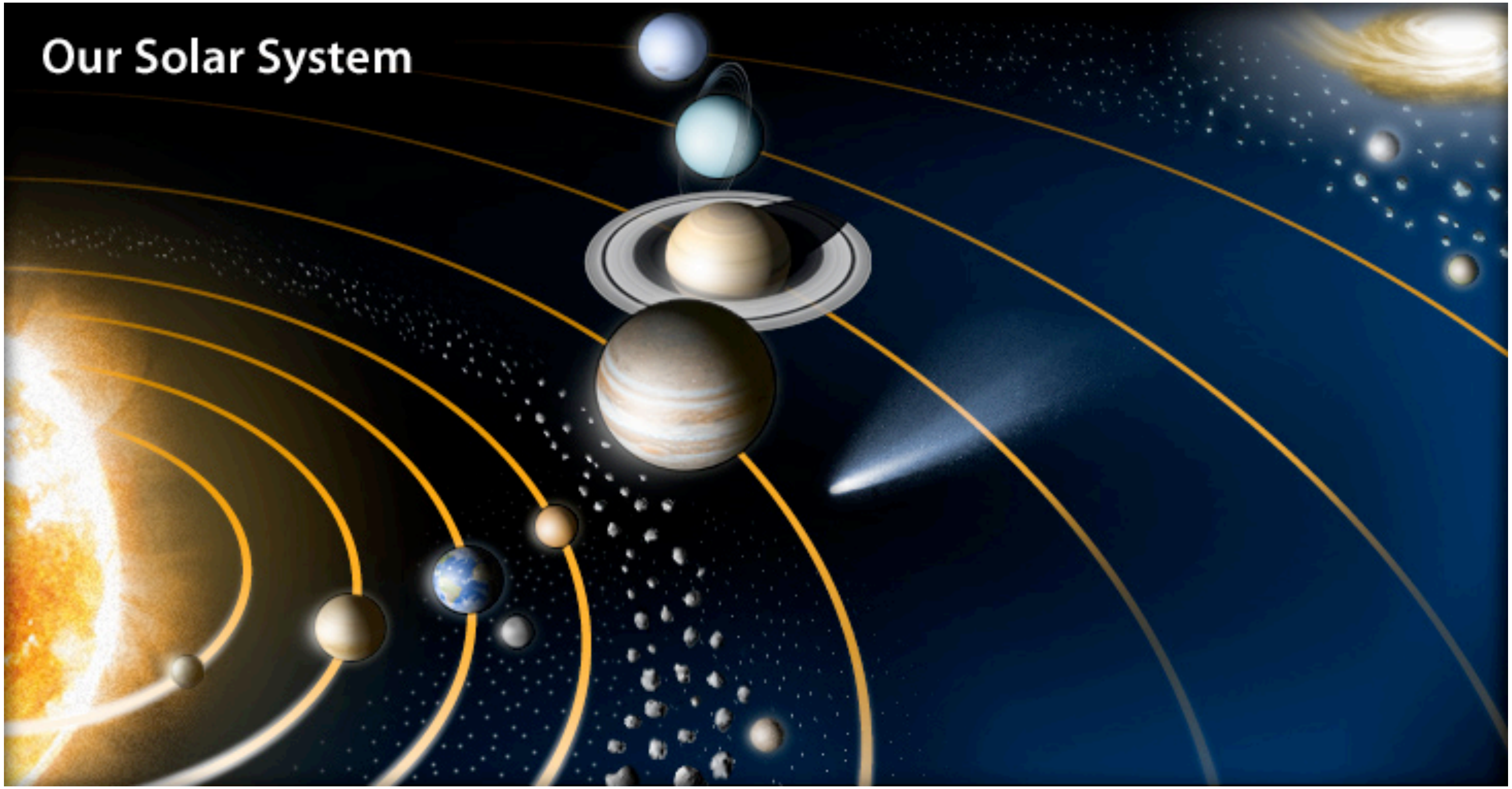

Artist image of the solar system
(NASA)

Venus case

- Hovenier (2012)

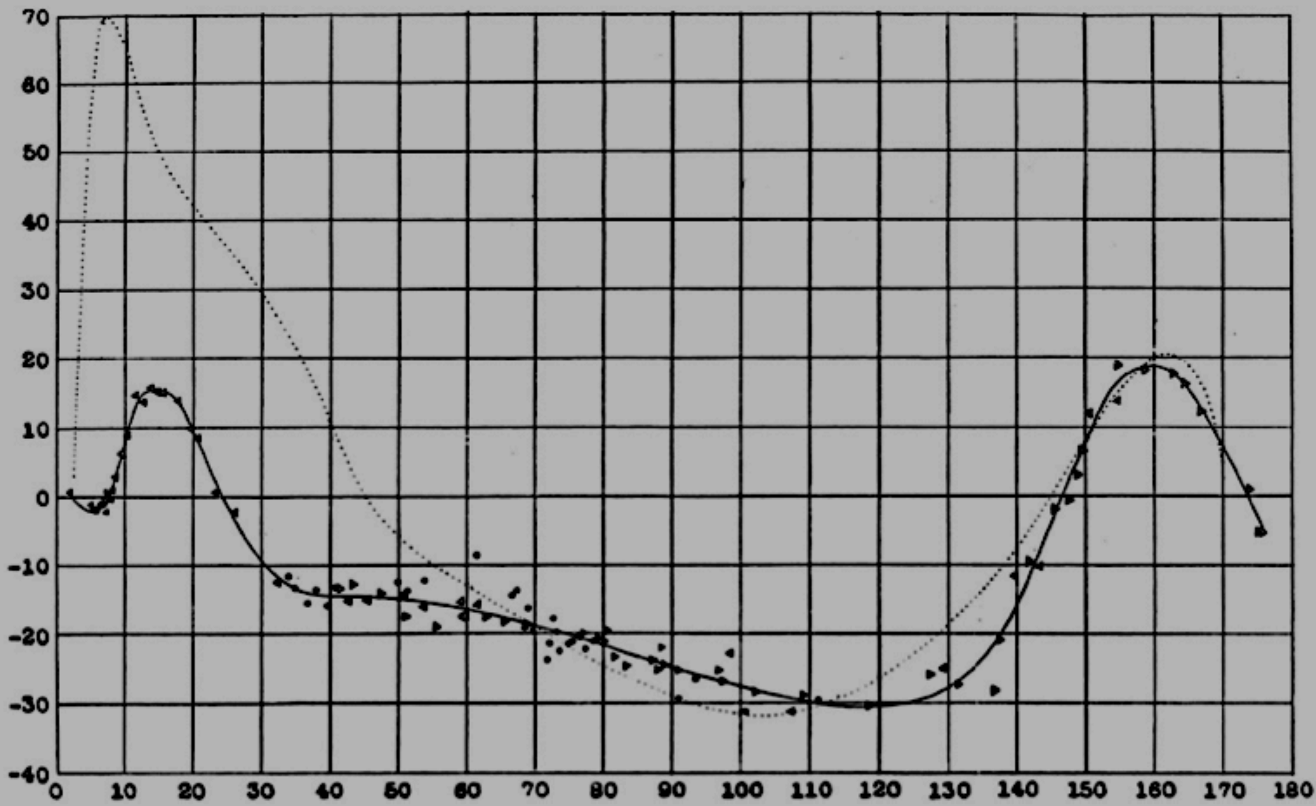

Fig. 1. The degree of polarization of the planet Venus in parts per thousand versus its phase angle in degrees according to Lyot [10]. The solid curve represents observations during different cycles. The dotted curve is a reduced experimental curve for water droplets. (After Lyot [10]).

Venus case

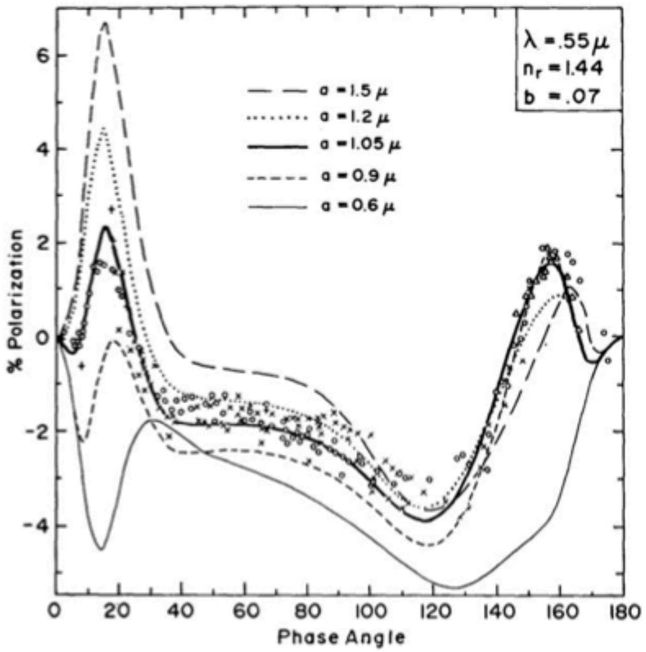

Fig. 2. The polarization of Venus at 0.55 μm. The symbols pertain to observations. The curves are the results of multiple scattering calculations for a thick atmosphere containing spheres with various effective radii (a) and one effective variance (b). The different curves show the influence of the particle size on the polarization. (After Hansen and Hovenier [19]).

- the cloud particles must be spherical because there is a rainbow feature in the polarization;
- the effective radius of the particles is 1.05 ± 0.10 μm with a narrow size distribution; the refractive index is 1.46 at 0.365 μm, 1.44 at 0.55 μm and 1.43 at 0.99 μm;

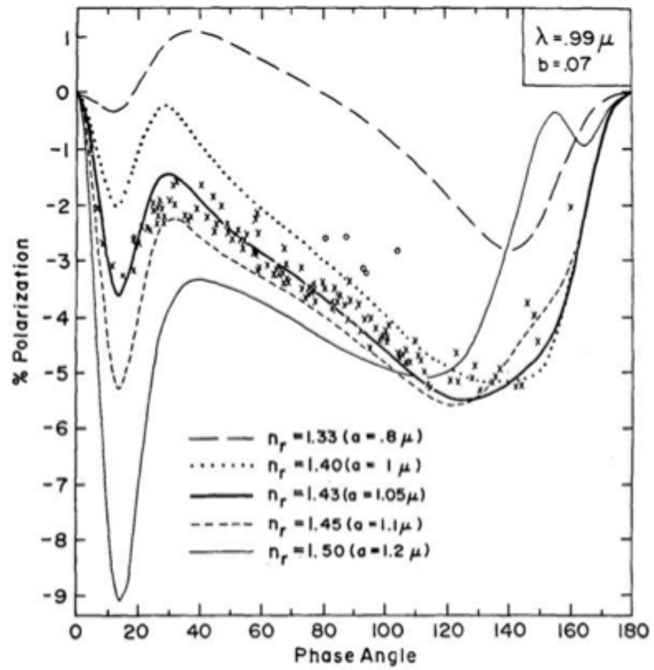

Fig. 3. As Fig. 2, but for a wavelength of 0.99 μm and theoretical curves for various refractive indices. The effective particle radius is selected in each case to yield closest agreement with the observations at all wavelengths. (After Hansen and Hovenier [19].)

- the wavelength dependence of the refractive index shows that the composition of the clouds is a strong aqueous solution of sulfuric acid with a concentration of about 75%;
- the influence of molecules above the cloud deck on the polarization at 0.365 μm shows that the top of the cloud layer is at about 50 mbar.

Still studied: Rossi et al. Study of Venus' cloud layers by polarimetry using SPICAV/Vex. EGU 2013

Jupiter and Saturn cases (Schmid et al. 2011)

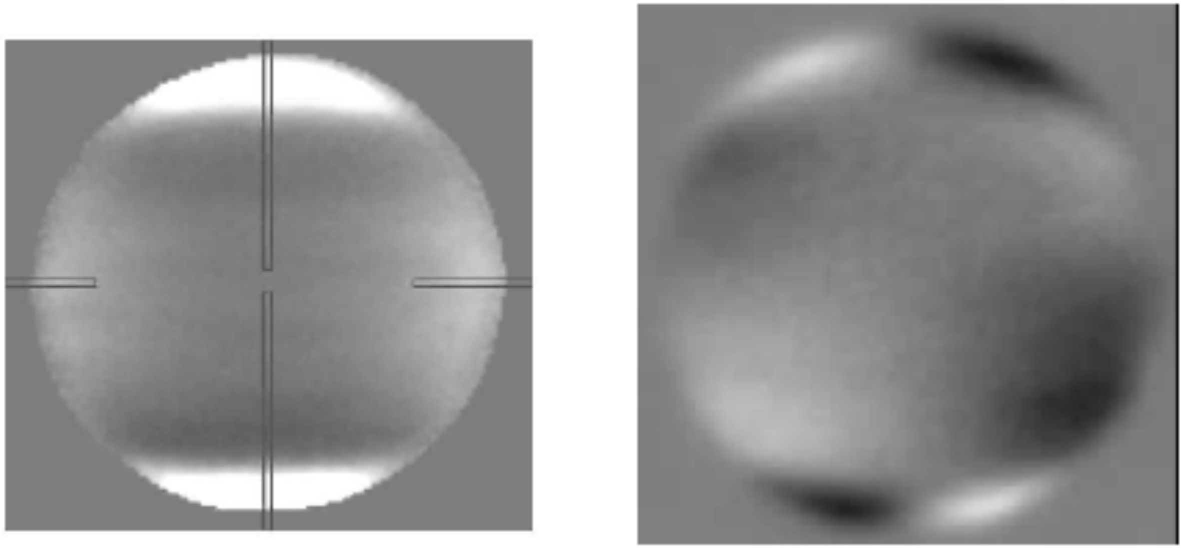

Fig. 1.— Q (left) and U (right) polarization flux images of Jupiter in a filter centered at 7300 Å taken with ZIMPOL in March 2003 at Kitt Peak. North is up and East is left. The grey scale is normalized to the central intensity and spans the range from −1.0 % (black) to +1.0 % (white). The lines in the Q-image indicate the slit positions for the spectropolarimetric observations with EFOSC2.

Radial polarisation

5. The radial polarization

The data are presented in the previous section as separate images of the Stokes Q and U flux instead of the polarized flux $p \times I = (Q^2 + U^2)^{1/2}$. The square of Q and U in the formula for the polarized flux introduces large systematic errors, if the absolute value of the measured signals $|Q|$ and $|U|$ is not significantly higher than the measuring noise ΔQ and ΔU. In our Uranus and Neptune data, there is $\Delta Q \approx |Q|$ (and $\Delta U \approx |U|$) in the middle of the planetary disk and between the positive and negative Q and U features. Therefore the use of the polarized flux $p \times I$ (or the normalized polarization p) as measuring parameter would lead to wrong results.

With radial Stokes parameters these problems can be avoided, and averaged (radial) polarization values for the limb polarization and the polarization as a function of radius can be derived without introducing systematic errors in the data reduction process. In particular, radial Stokes parameters are well-suited for characterizing a centro-symmetric polarization pattern.

The radial Stokes parameters Q_r and U_r describe the polarization in radial and tangential direction on the planetary disk. Q_r and U_r are given by

$$\begin{aligned} Q_r &= +Q\cos 2\phi + U\sin 2\phi \\ U_r &= -Q\sin 2\phi + U\cos 2\phi, \end{aligned}$$

where ϕ is the polar angle of a given position (x, y) (equivalent to (α, δ)) on the apparent planetary disk (disk center (x_0, y_0)) with respect to the North direction:

$$\phi = \arctan \frac{x - x_0}{y - y_0}.$$

$Q_r > 0$ is equivalent to a radial polarization or a polarization perpendicular to the limb, while $Q_r < 0$ indicates a tangential polarization component. U_r describes the polarization in the directions $\pm 45°$ with respect to the radial direction.

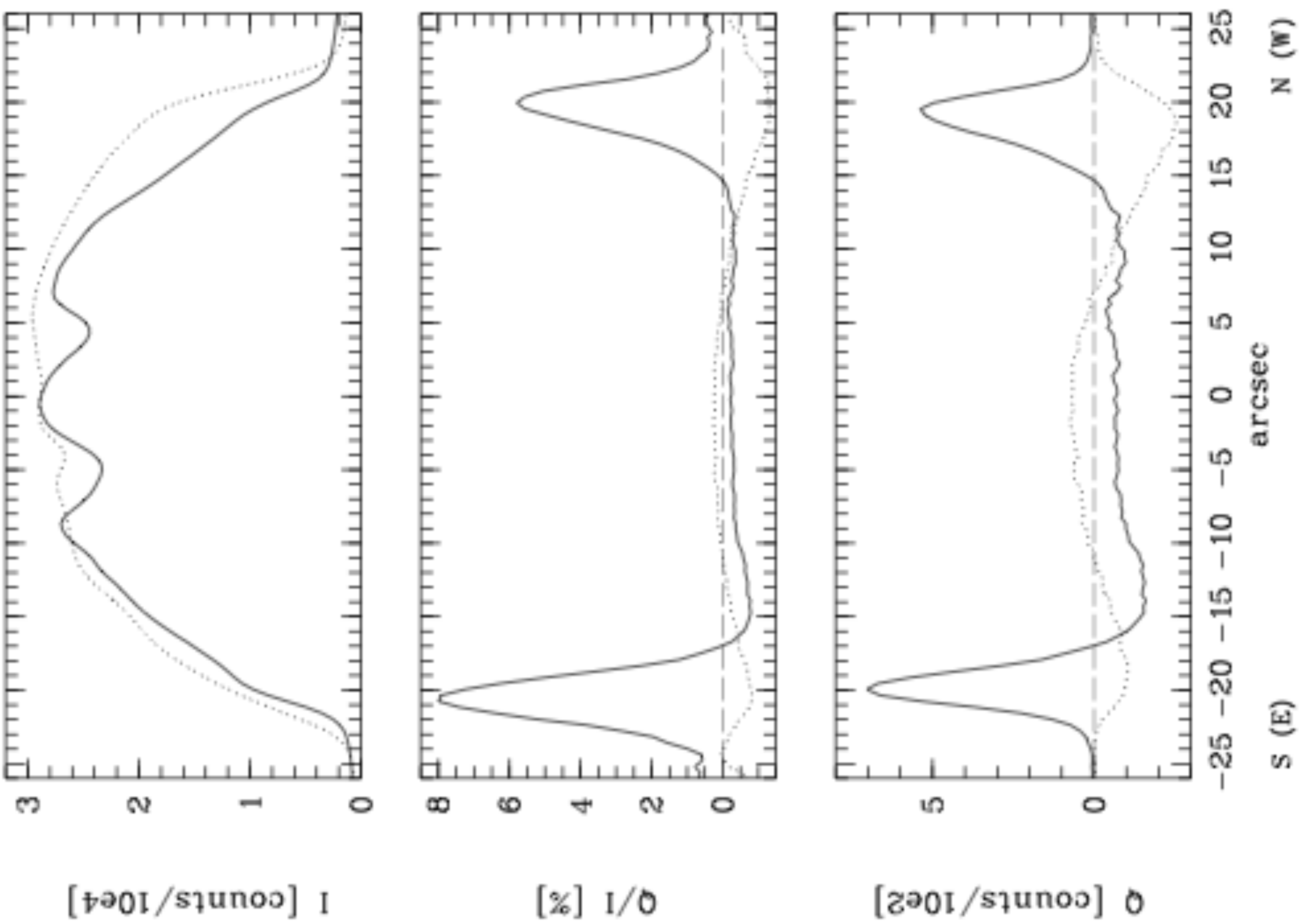

Fig. 2.— Observations of Jupiter from March 2003. Polarimetric profiles in N-S (full line) and E-W (dotted line) direction, taken in the 7300 Å filter with ZIMPOL. The top panel shows the intensity I, the middle panel the fractional (radial) polarization Q_r/I, and the bottom panel the polarization flux Q_r.

CH4 absorption bands

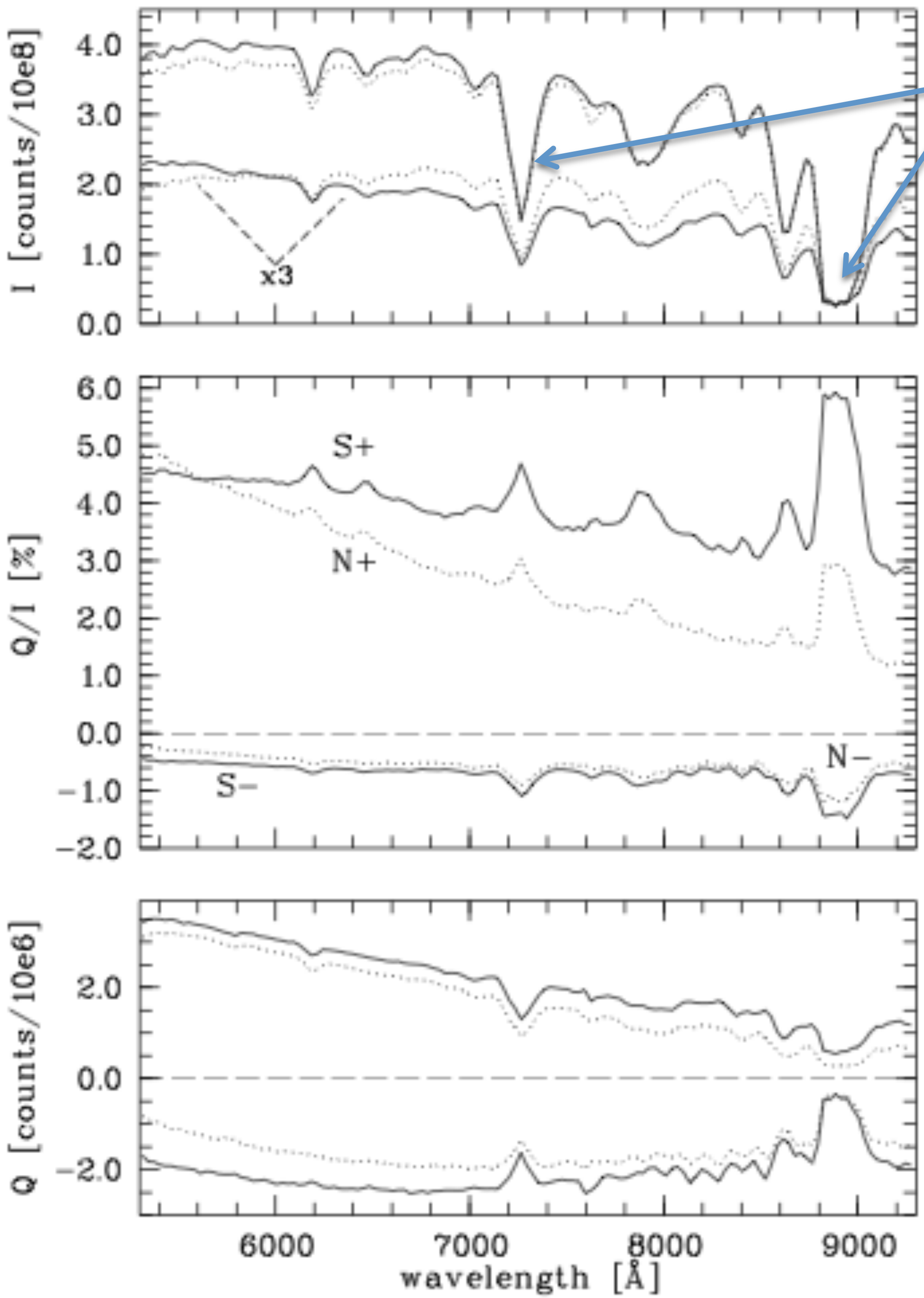

Fig. 4.— Spectropolarimetry of Jupiter for the S+, S− (solid lines) and the N− and N+ (dashed lines) regions as defined in Fig. 3. The intensity $I(\lambda)$ for the polar region S+ and N+ are multiplied by a factor of 3 with respect to S− and N− for visibility reasons. The middle panel gives $Q_r/I(\lambda)$ and the bottom panel the polarization flux Q_r.

N+ and S+ corresponds to Latitude: 73°
S- and N- to mid latitudes (out of the polar haze)

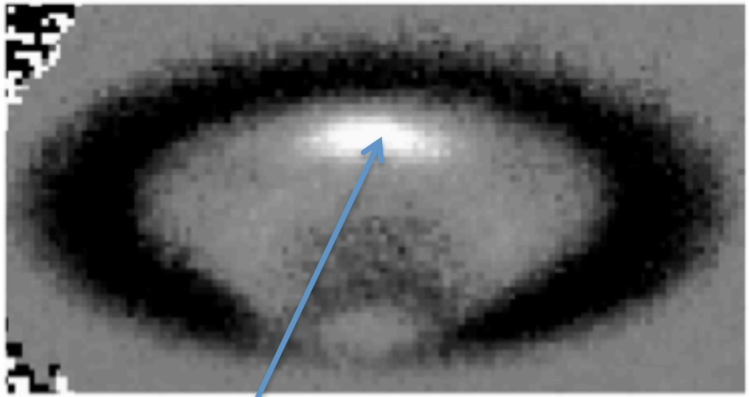

Fig. 7.— ZIMPOL Stokes Q-flux image of Saturn, obtained in the methane 730 nm filt
In the south the planet occults the ring, except for a small rim with a width of about 1.5

Transient polarisation
feature: unexplained.

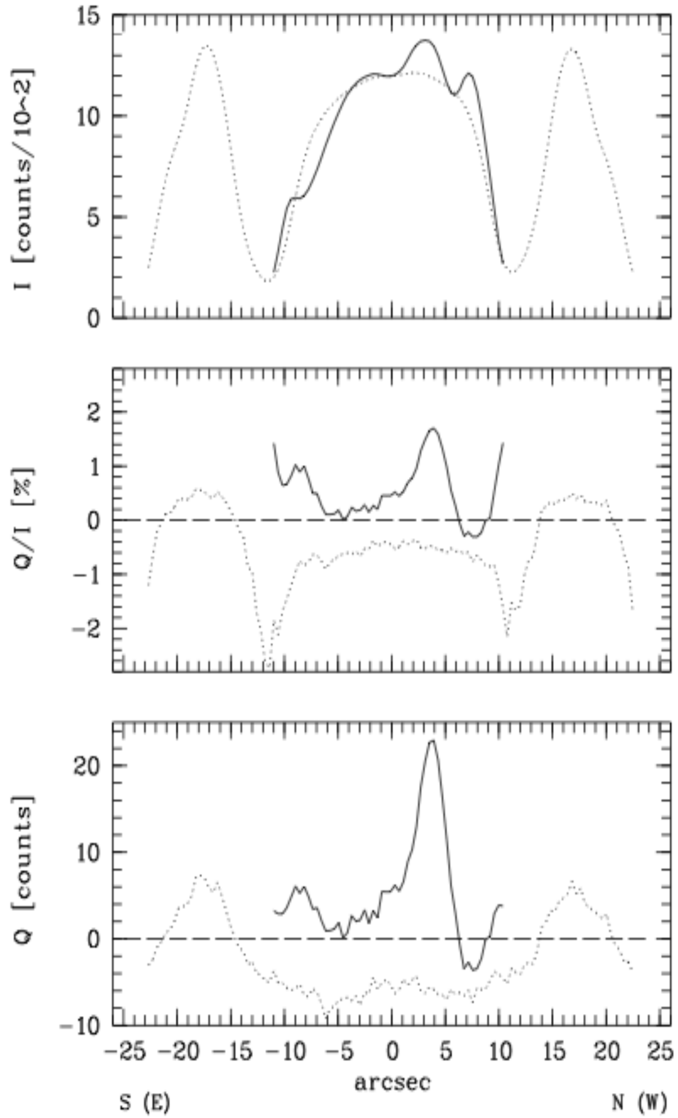

Fig. 8.— Saturn N-S (full line) and E-W profiles (dotted line) for the intensity (top), the fractional radial polarization Q_r/I, and the Q_r polarization flux for the wavelength λ7300Å.

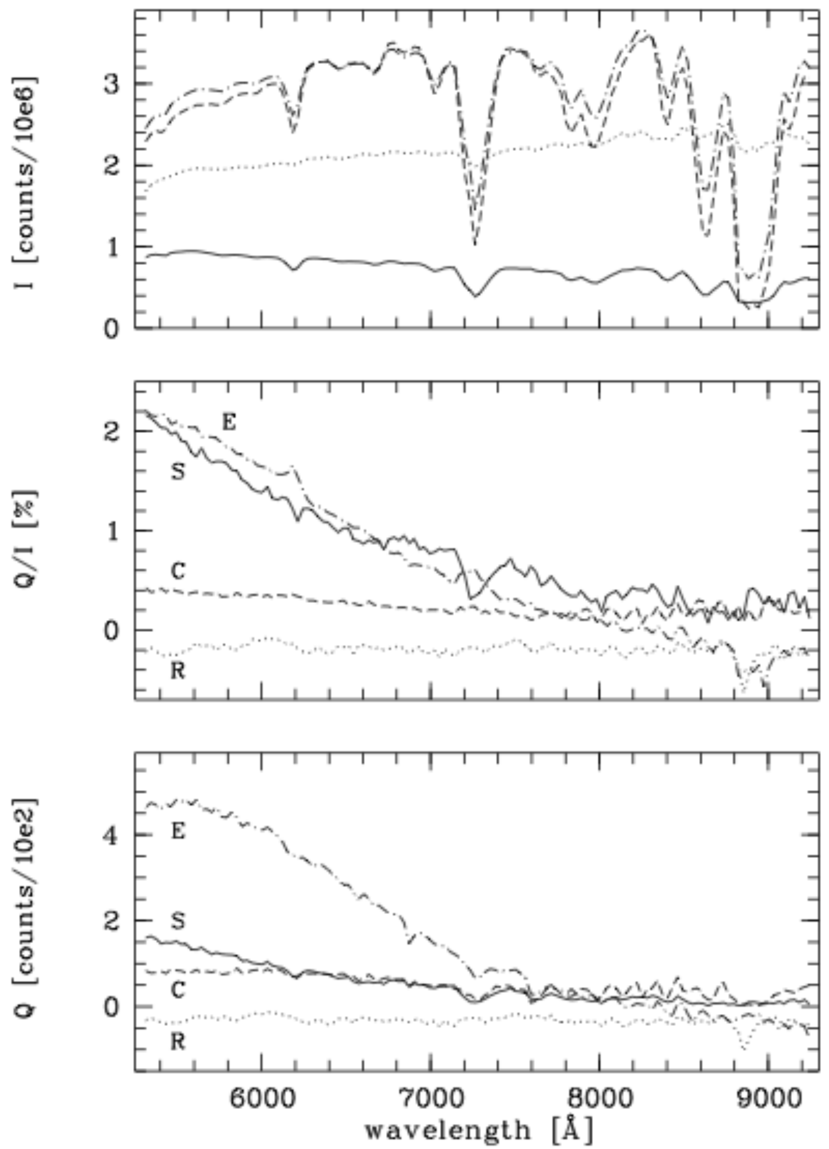

Fig. 10.— Spectropolarimetry for the four regions of Saturn: south pole (solid line), center (dashed line), equator (dot-dashed line), and ring (dotted line). Top panel: intensity spectra $I(\lambda)$ (counts). Middle panel: fractional polarization $Q_r/I(\lambda)$. Positive is parallel to the slit and negative is perpendicular. Bottom panel: polarized flux $Q_r(\lambda)$.

Uranus and Neptune (Schmid et al. 2006)

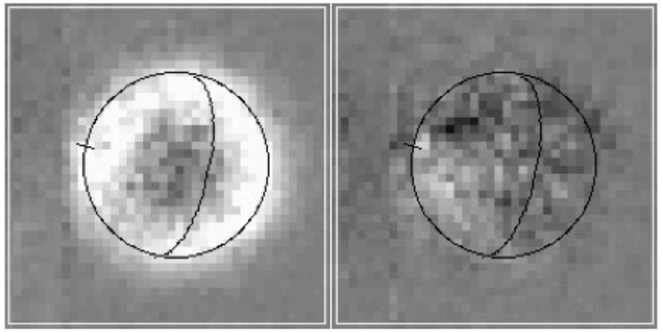

Fig. 4. Radial Stokes Q_r (*left*) and U_r (*right*) for Uranus in the *i*-band. The grey scale is normalized to the peak intensity I_{peak} and goes from −0.5% (black) to +0.5% (white).

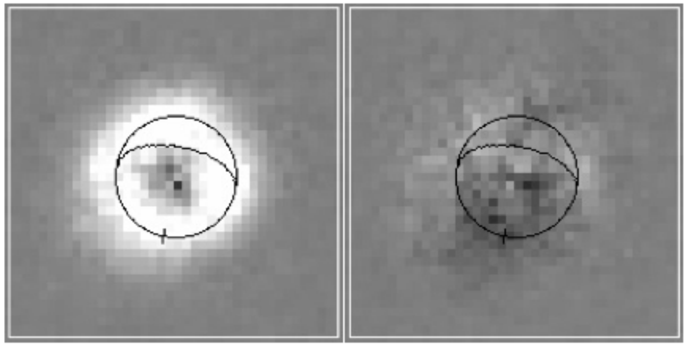

Fig. 5. Radial Stokes Q_r (*left*) and U_r (*right*) for Neptune in the *R*-band. The grey scale is normalized to the peak intensity I_{peak} and goes from −0.5% (black) to +0.5% (white).

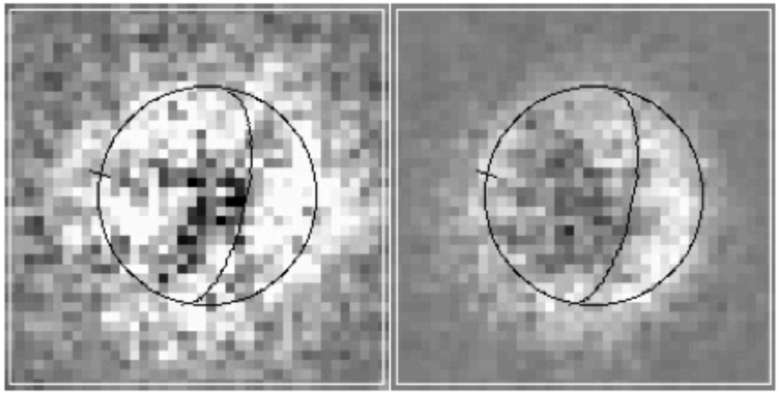

Fig. 6. Radial Stokes parameter Q_r for Uranus in the narrow λ 673 nm filter (*left*) and the *z* filter (*right*); grey scale as in Fig. 5.

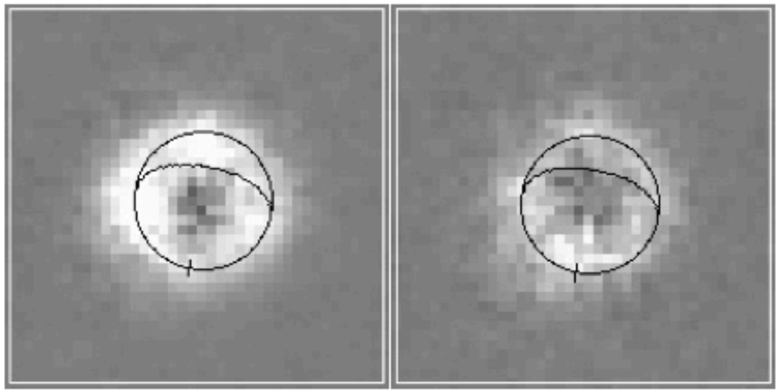

Fig. 7. Radial Stokes parameter Q_r for Neptune in the *i* (*left*) and *z* filters (*right*); grey scale as in Fig. 5.

8. Seeing corrections

The seeing-limited resolution of our planet observations causes a polarization cancellation effect. This has to be taken into account for interpreting the polarization properties of Uranus and Neptune. Due to the seeing, the opposite polarization components $+Q$ and $-Q$ overlap and cause a reduction in the resulting net polarization. In the most extreme case of an unresolved centro-symmetric planetary disk, the polarization cancellation would be perfect and only a zero net polarization level could be measured. Of course the compensation effect is stronger for Neptune than for Uranus because of the smaller apparent diameter of the former planet.

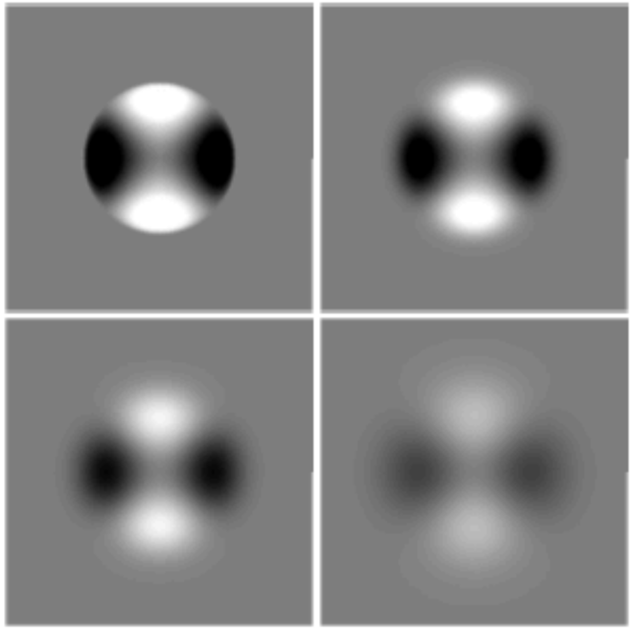

Fig. 10. Modeling of the degradation of the polarization Q due to the cancellation of opposite polarization components $+Q$ and $-Q$ caused by the seeing limited resolution; **a)** no seeing, **b)** seeing 0.3 $R_{\rm planet}$, **c)** seeing 0.5 $R_{\rm planet}$, and **d)** seeing 0.8 $R_{\rm planet}$. The grey scale spans for all panels the range from −1% (black) to +1% (white) of the peak intensity of the initial (no seeing) intensity image.

In Sect. 2 we estimated a seeing of 0.8″ for our observations. The uncertainty in the estimated seeing is about ±0.1″. Thus the seeing degradation factor for the integrated radial polarization $\langle Q_{\rm r}\rangle_{\rm seeing}/\langle Q_{\rm r}\rangle_0$ is roughly 0.82 for Uranus (seeing 0.46 $R_{\rm planet}$) and 0.65 for Neptune (seeing 0.71 $R_{\rm planet}$). For an estimate of the intrinsic radial polarization $\langle Q_{\rm r}/I\rangle$, the values derived from the observations (Table 2) have to be multiplied by the inverse values, thus with 1.22 and 1.54 for Uranus and Neptune, respectively.

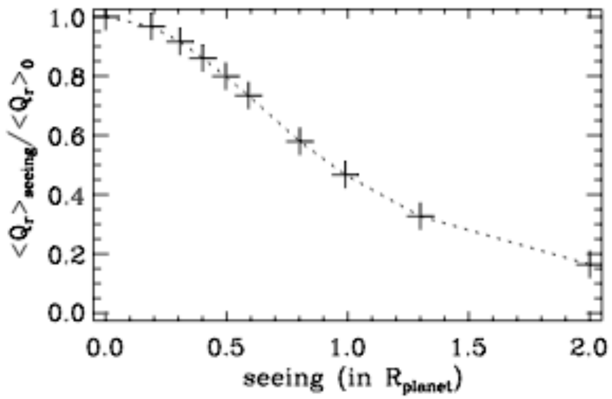

Fig. 11. Measurable radial polarization $\langle Q_{\rm r}\rangle_{\rm seeing}$ relative to the initial radial polarization $\langle Q_{\rm r}\rangle_0$ as a function of the seeing for a planet with a (semi-infinite, conservative) Rayleigh-scattering atmosphere. The seeing (FWHM) is expressed in units of the radius of the planetary disk.

Giant planets: Rayleigh scattering or aerosols (or both)

- Limb polarisation: 2 diffusion problem but rayleigh scattering

- The general tendency for the limb polarization to be higher at shorter wavelengths is caused by the wavelength dependence of the Rayleigh scattering cross section, which increases rapidly towards the blue (like $\propto 1/\lambda^4$).
- The polarization in the red continuum, i.e. in the λ = 673 nm-filter for Uranus and R-band for Neptune, is significantly lower than expected for a semi-infinite atmosphere. The relatively low polarization can be explained by a Rayleigh scattering layer above a reflecting, optically thick cloud layer.
- In the strong methane absorption bands in the red and near-IR, the photons are absorbed predominantly before they reach the cloud tops. In this case the polarization can be roughly approximated with a semi-infinite Rayleigh-scattering atmosphere with a low single-scattering albedo $\omega \lesssim 0.5$.

Giant planets: Rayleigh scattering or aerosols (or both)

- Polar Haze: aerosols

The free parameters of our model are: the albedo cloud layer A_S assumed to be a grey Lambert surface, the optical thickness of the haze layer τ_h, and the haze parameters, which are single scattering albedo ω_h, single term Henyey-Greenstein asymmetry parameter g_h, and maximum polarization for right angle scattering p_h (see Braak et al. 2002). The polar model is independent of latitude, but the incidence and viewing angles produce a latitude dependence in the reflected polarization and intensity.

Our model fit is not unique. However, many parameters are already well constrained. From the parameter space explored by us it seems very likely that the asymmetry parameter lies in the range $0.8 < g_h < 0.5$ and the single scattering polarization is $p_h > 0.8$.

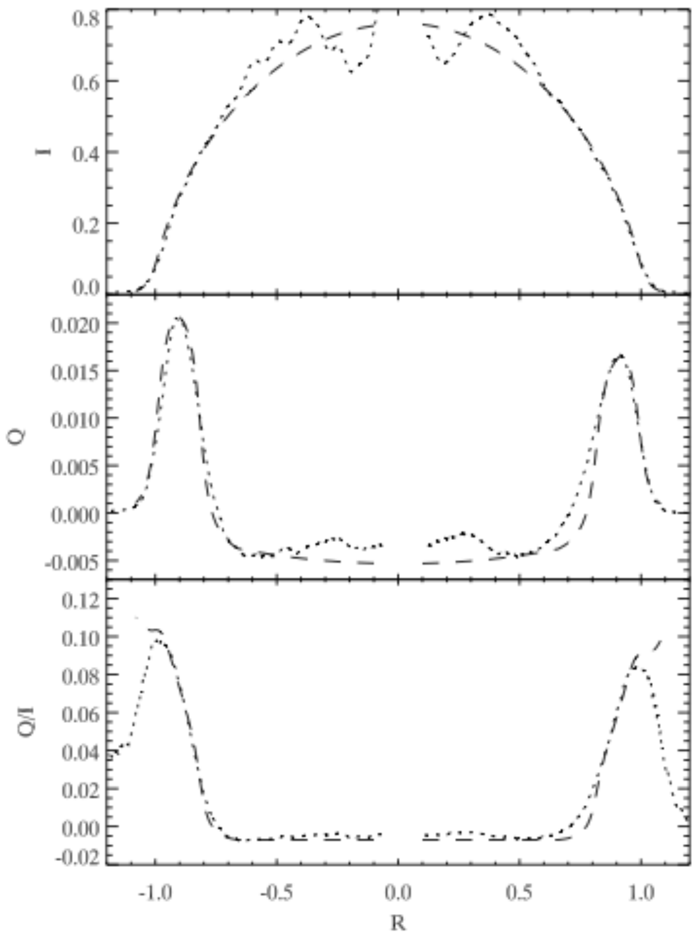

Fig. 11.— Comparison of the model fit (dashed line) with the observed 6000 Å N-S profile (dotted line) of Jupiter.

Titan: very high polarisation levels (Tomasko et al. 2008: 2009)

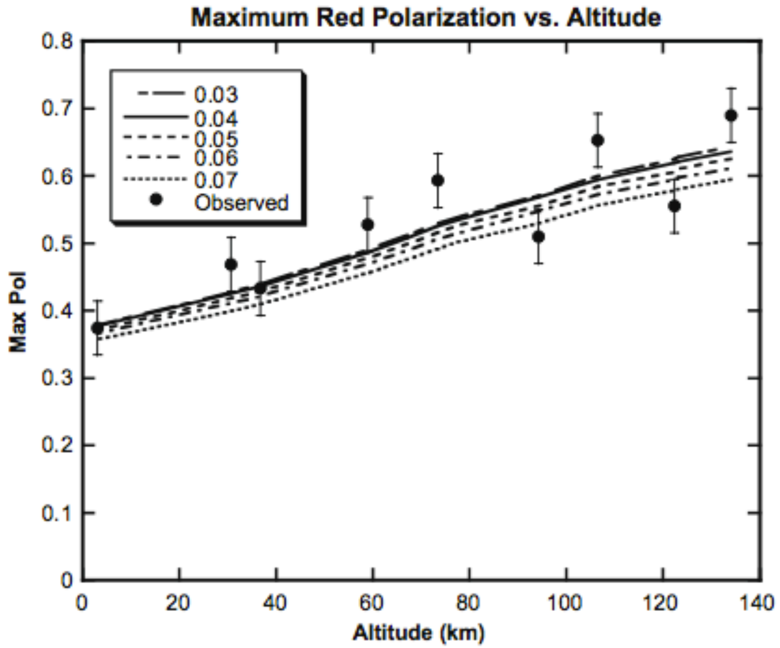

Fig. 18. The maximum values of linear polarization measured in the red channel (points) compared to models containing monomers of radii from 0.03 μm to 0.07 μm, as labeled. The error bars on the measured points reflect the range resulting from reductions using a range of probe attitudes. The range of probe attitudes shown is a few degrees in azimuth, tip toward the Sun, and tip in the orthogonal direction, amounts that are possible within other known constraints. Note that within the range of uncertainty of the observations, models with any of these monomer radii would give acceptable fits to the observations.

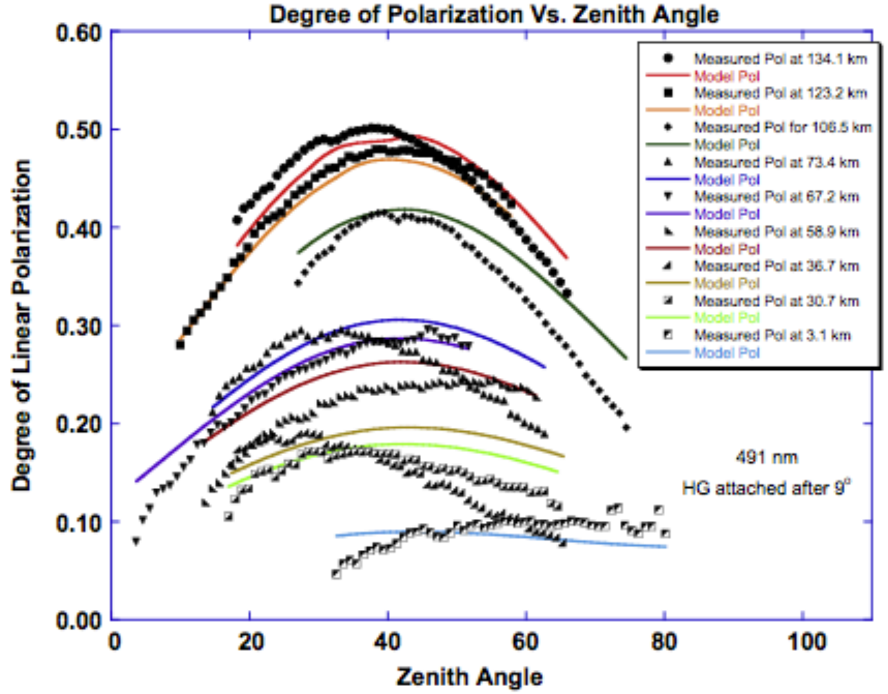

Fig. 20. Blue polarization measurements (points) compared to models (curves) as functions of zenith angle for nine altitudes, as labeled. Note that the maximum values of the measured and model values agree to within ±0.02, while the shape of the curves sometimes drifts off at the limits of the zenith angle range where the dependence on probe attitude is greatest.

Determination of light scattering by a specific aggregation of spheres can be done with code that is publicly available (http://www.giss.nasa.gov/~crmim/t_matrix.html). The raw output of such an exercise is not used for two reasons. First, this is a computationally intensive process. To perform a trial of a set of parameters describing Titan's aerosols, the time spent determining single-scattering

Aller à la page 707

Table A1
[illegible]rameters

Parameter	Meaning	Tested range[a]
D_f	Fractal dimension	2
N	Number of monomers per aggregate	2–1024
$X_{monomer}$	Monomer size parameter ($2\pi a_{monomer}/\lambda$)	10^{-4}–1.5
n_r	Real part of index of refraction	1.3–2
n_i	Imaginary part of index of refraction	0–0.7

[a]Not all combinations within the tested range are valid: in particular, large N is not paired with large $X_{monomer}$.

properties would exceed that spent determining multiple-scattering results by many orders of magnitude. The time and computer requirements required increase dramatically with aerosol size. Second, an aggregate of N spheres can be put together in a continuous variety of ways. A model of a specific aggregate may not be representative of an average of many aggregates. Scattering properties can therefore change discontinuously as different specific aggregates are compared. Other formulations (Botet et al., 1997; Rannou et al., 1999) average prior to performing scattering calculations, making assumptions about the effects of non-linearity in the scattering.

A parameterization is a useful alternative to exact computations. First, it can be executed quickly. Second, the output can be made to vary continuously (or smoothly for integer input) with the input. The parameterization chosen takes as input five parameters (see Table A1) describing the size, shape, and composition of the aggregate. The following is intended as a guide to reproducing the results here.

The parameterization scheme is (1) coherent superposition of scattering by monomers; (2) linear superposition of absorption and; (3) correction factors near unity that are functions of $X_m = 2\pi r_m/\lambda$, N, and the index of refraction. The first component is a function only of the assumptions of monomer scattering properties (here Mie scattering by identical spheres) and the geometric arrangement of those spheres. The last component accounts for most of the complexity, empirically modeling multiple interactions (light scattered by one monomer and absorbed by another, or scattered twice) and non-linear effects of monomers nearby compared to the wavelength of light. Coherent backscatter of particles with X_m near 1 is seen in the T-matrix results, but is not implemented in the parameterization.

Cirrus: POLDER (Chepfer et al. 1998)

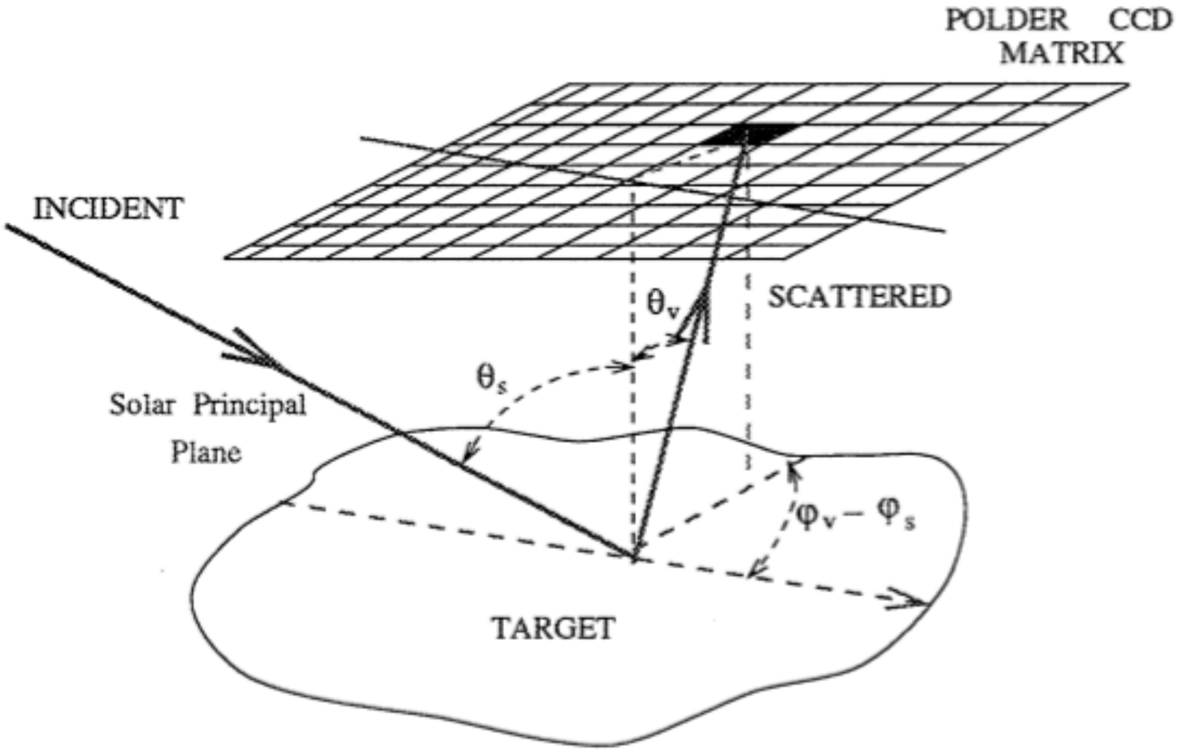

Fig. 1. Viewing geometry of POLDER. Each element of the target is identified on the CCD matrix with the couple of angles (θ_V, $\varphi_V - \varphi_S$). The solar principal plane is drawn as one straight line on the matrix.

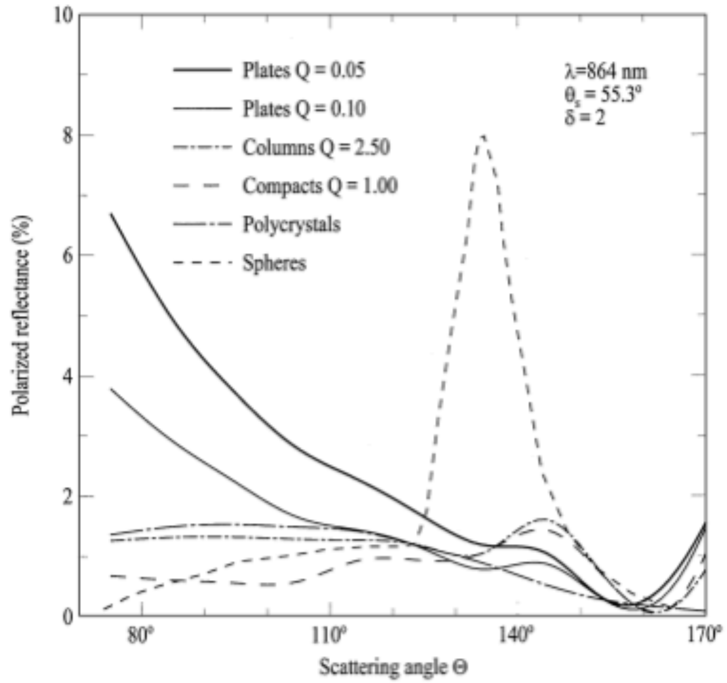

. Sensitivity of the polarized reflectance to the ice crystal shape at 864 nm, for a cirrus cloud optical thickness of $\delta = 2$, and a solar zenith angle of $\theta_s = 55.3°$.

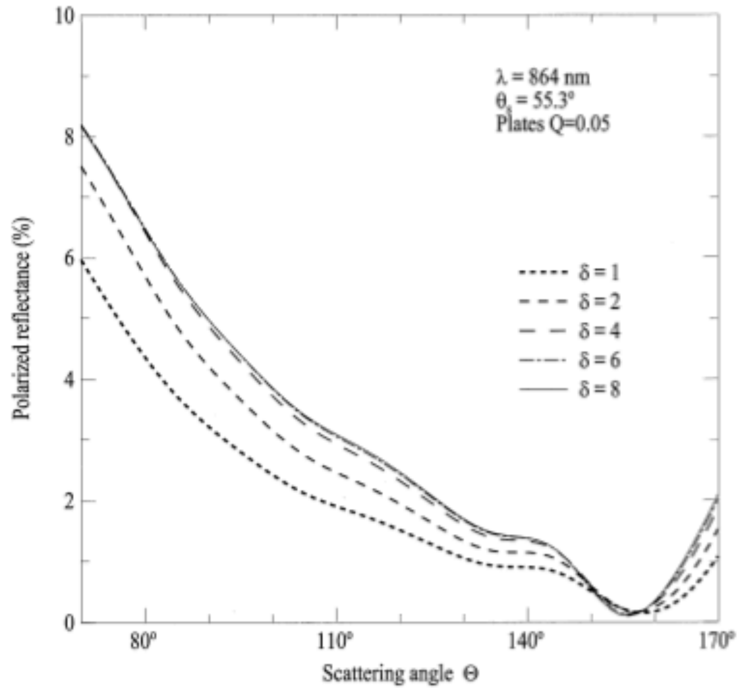

. Sensitivity of the polarized reflectance at 864 nm to the cirrus cloud optical thickness for $\theta_s = 55.3°$. Case of hexagonal plates with aspect ratio $Q = 0.05$.

Auroral light polarisation

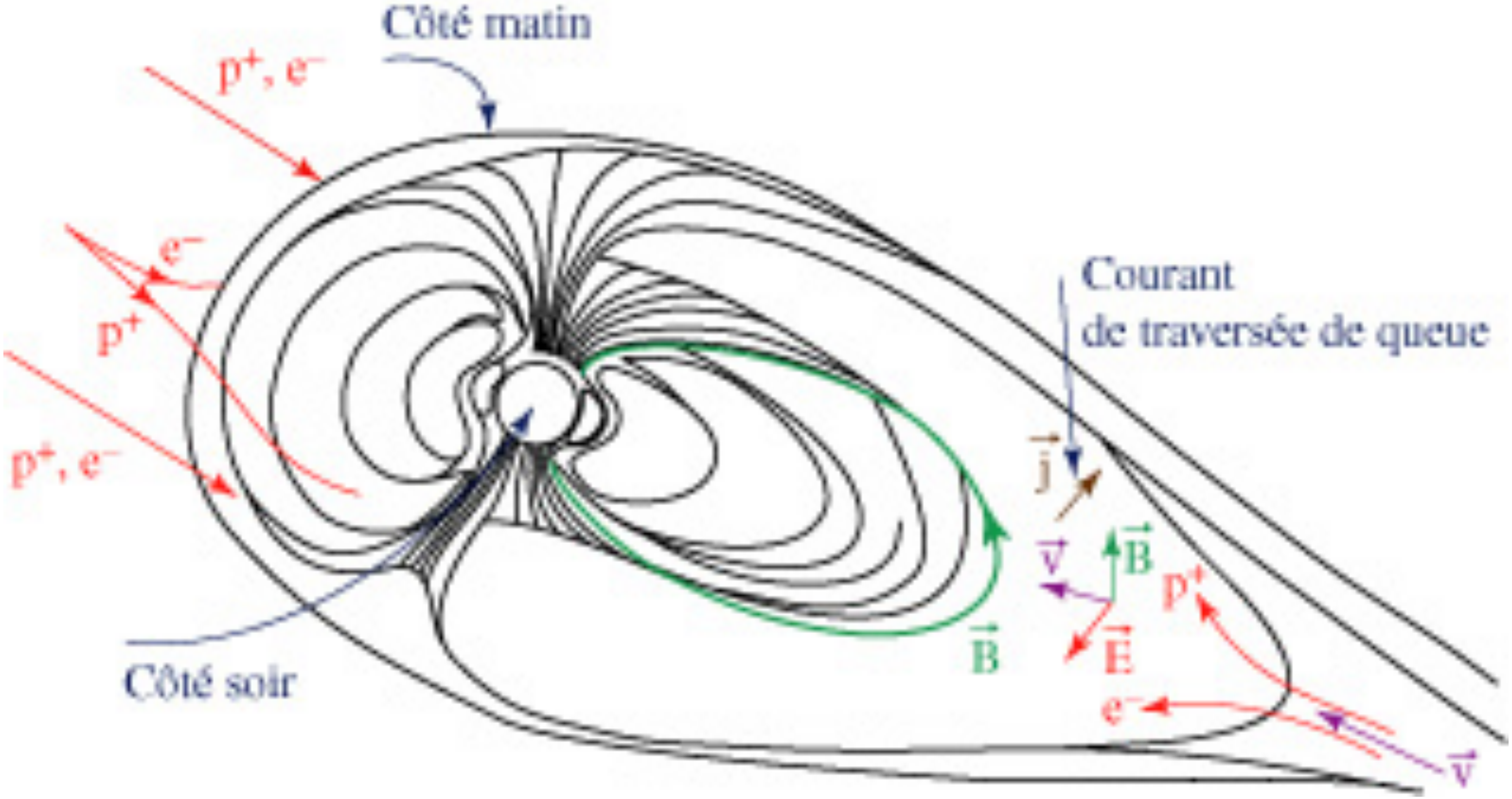

The red line…

Which lines: O^1D
(630nm; Lilensten et al 2006)

Mesurable: Yes. 2nd most intense in the auroral spectra.

Measurement: SPP Instrument (With UIO). Pb of the location.

ab initio calculation:
Bommier et al (2011): pola rate variation with the energy of the electrons.
<u>Work in progress : collisionnal depolarisation</u>

New campaigns (KHO, Hornsund).
Mainland Norway (Inside the oval)
Ellesmere Island Very high magnetic latitudes

Polarised signal extraction: yes but strong pb with the light polution (Lilensten et al. 2008).
<u>Confirmed in 2011 (Barthelemy et al.2011)</u>

Interpretation: work in progress.
Sensitive to the energy of the electrons, to the local density, to …?

The red line polarisation

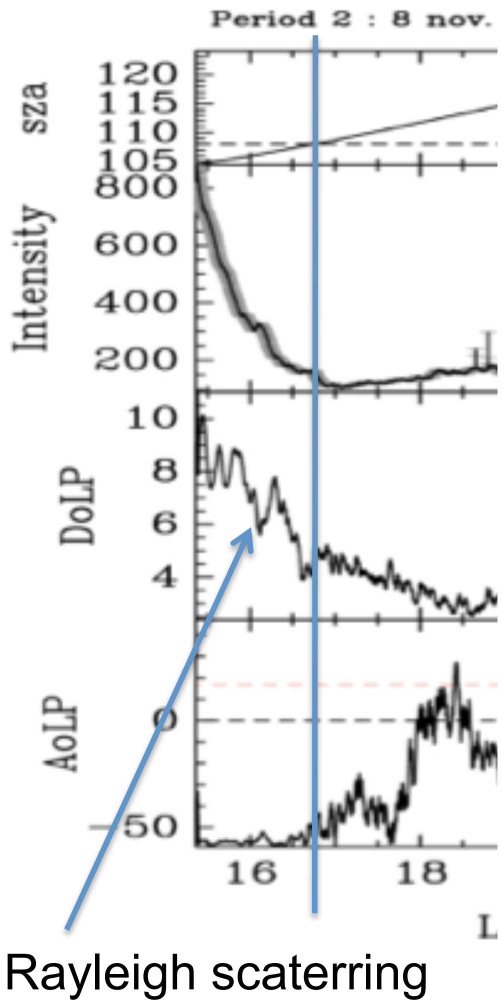

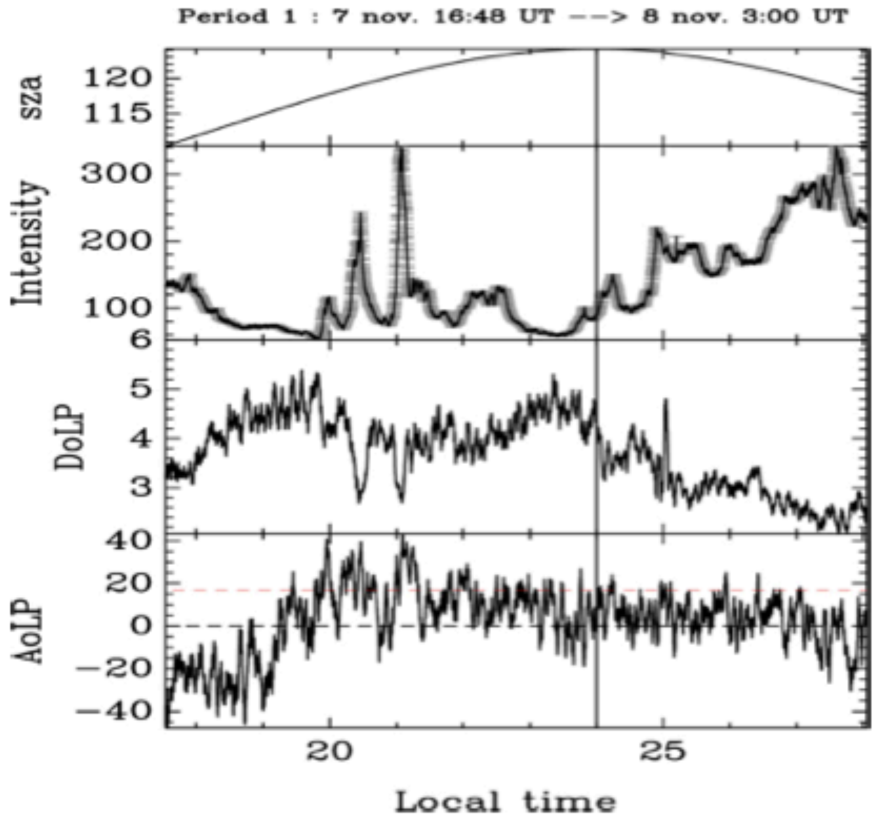

Fig. 7. *Upper panel*: solar zenith angle in degrees. *Lower panel*: total intensity of the red line in count rates (see text). The error bars are given in gray. The next two panels below show the DoLP in % and the AoLP in degrees. 0° is vertical and 90° is horizontal. The dashed red line represents the measured instrumental AoLP. The vertical full line indicates midnight.

-Polarisation degree as a function of the particles energy.)

- -Polarisation degree very stable around 17% (strong difference with the data)
- -Direction // to B (coherent with the data)

- -but

-Collisionnal Depolarisations

-Secondary electron role

-Angle distribution function

- - Work in progress (V. Bommier et al.).

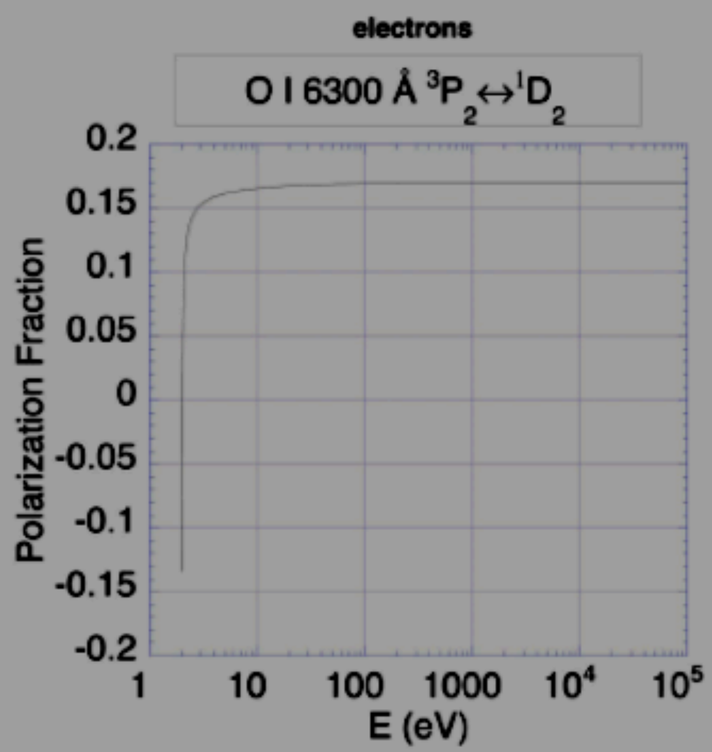

Fig. 3. Impact polarization (linear polarization) due to line collisional excitation by directive electrons, as a function of the energy of the colliding electron, which is assumed to propagate along Ox, the radiation being observed along Oz. A positive polarization means *radial* polarization, *i.e.* oriented also along Ox, lying inside the scattering plane. A negative polarization means *tangential* polarization, *i.e.* oriented along Oy, perpendicular to the scattering plane.

Calculation (Bommier et al. 2011)

- Green line non polarizable (J=0). Red line potentially (J=2).

2 Atomic physics: the theoretical impact polarization

2.1 The O I 6300 Å line: a doubly forbidden line

As stated above, the upper level is $2s^2 2p^4\ {}^1D_2$ and the lower level $2s^2 2p^4\ {}^3P_2$. As both levels belong to the fundamental configuration, the first non-zero term of the electron-atom Coulomb interaction potential is the quadrupolar term. In the general case of a perturber of charge Z_p interacting with an atom (or ion) of charge Z having N electrons, the interaction potential results from the Coulomb interaction

$$V = \frac{Z_\mathrm{p}(Z+N)e^2}{r_\mathrm{p}} - Z_\mathrm{p} e^2 \sum_{i=1}^{N} \frac{1}{r_{ip}}\,, \tag{1}$$

where p refers to the perturber and i refers to the i-th atomic electron. It can be developed in multipolar components, and the restriction to the quadrupolar one (in the case of the long-range approximation, and assuming a single active electron) leads to (case of a neutral atom $Z=0$)

$$V = -\sum_{\mu=-2}^{+2} \frac{4\pi Z_\mathrm{p} e^2}{5} \frac{r_i^2}{r_\mathrm{p}^3} Y_\mu^2(\hat{r}_\mathrm{p}) Y_\mu^{2*}(\hat{r}_i)\,, \tag{2}$$

where $r_{\mathrm{p},i}$ is the distance of the perturber or atomic electron to the nucleus ($r_{i\mathrm{p}}$ being the distance between the perturber and the atomic electron), and $\hat{r}_{\mathrm{p},i}$ are the two director angles. Y_μ^2 is a spherical harmonic.

This quadrupolar potential corresponds to the interaction between the atom and the incoming electron. As for the radiation emission that follows, the first non-zero contribution comes from the dipolar magnetic interation with the vacuum. Concerning the emitted polarization, the computation is the same as for the usual dipolar electric emission except for the sign that has to be reversed (see for instance Sahal-Bréchot, 1974, Eq. 26).

As previously stated, the second reason that makes this line a forbidden one, is the fact that the transition implies a spin flip from a triplet level to a singlet level.

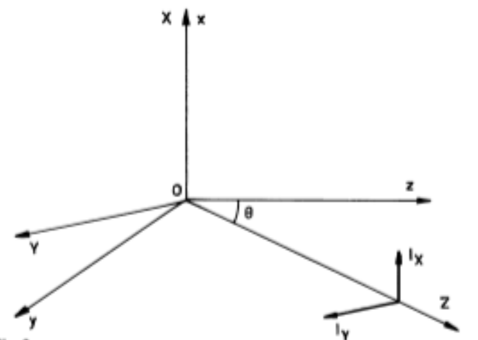

Fig. 2

We detect the vibrations in the plane XOY; that the principal directions of the vibrations are towards OX and OY, follows from the choice of the axes. The corresponding intensities are denoted by I_X and I_Y. By definition the total intensity of the line is

$$I_\mathrm{tot} = I_X + I_Y\,, \tag{26}$$

and the polarization degree

$$\tau = \varepsilon \frac{I_X - I_Y}{I_\mathrm{tot}}\,. \tag{26}$$

Calculation (Bommier et al. 2011)

2.2 Taking into account the triplet-singlet transition

The total system atom+perturber being isolated, the collision occurs within the conservation of the kinetic momentum of the total system. As usual, we neglect the atomic fine structure during the collision, because the collision time is so short that the fine structure energy differences may be neglected within the Heisenberg uncertainty principle. In other words, the spin has no time to rotate during the collision time. Thus, the collision occurs with the separate conservation of the total angular momentum L^{T} and of the total spin momentum S^{T}. Considering that the atomic lower level spin is $S = 1$

and the incoming electron spin is $s = 1/2$, two values are possible for S^T in the initial state. They are $S_1^{\mathrm{T}} = 1/2$ and $S_2^{\mathrm{T}} = 3/2$, following the laws for kinetic momentum addition in Quantum Mechanics. Considering now the final state, the atomic upper level has $S = 0$ and the outgoing electron has $s = 1/2$, so that $S_1^{\mathrm{T}} = 1/2$ remains compatible with this final state. Thus, the excitation of the $^1D_2$ state from the $^3P_2$ one is possible by electron impact, whereas it is forbidden by radiation absorption.

Anticipating the semi-classical development, it can be asserted that this development concerns the angular aspects of the problem depending on the different Zeeman sublevel transitions, whereas the line oscillator strength factorizes. For radiative transitions this oscillator strength is very small because the line is forbidden, which is not the case of the collisional cross-section. In this respect, we scaled our semi-classical result on the result of the quantum calculation at one given energy (here 68 eV for the incoming electron). From Barklem (2007) we received the dimensionless quantity (private communication)

$$\Omega = 1.72 \text{ at } 68 \text{ eV}, \tag{3}$$

which is related to the cross-section Q by

$$\frac{Q}{\pi a_0^2} = \frac{1.72}{5} \times \frac{1}{9} = 0.038222, \tag{4}$$

a_0 being the Bohr radius. The results of our theory that we present in Fig. 1 below have been scaled to this value at 68 eV, and it can be seen that Fig. 1 top left of Barklem (2007) agrees with our Fig. 1 (bottom) for all energies. 68 eV is not close to the threshold energy 1.967 eV, where the quantum result may be perturbed by sharp resonances.

In the time dependent perturbation theory, the transition probability from the $\alpha = |jm\rangle$ state to $\alpha' = |j'm'\rangle$,

$$P_{\alpha\alpha'}(\rho, \mathbf{v}) = \frac{1}{\hbar^2}\left|\int_{-\infty}^{+\infty} V_{\alpha\alpha'} e^{i\omega_{\alpha\alpha'}t} dt\right|^2 , \tag{5}$$

is

$$P_{\alpha\alpha'}(\rho, \mathbf{v}) = \frac{Z_p^2 e^4}{\hbar^2}\frac{4\pi}{5} a_0^4 Q(2j+1)\begin{pmatrix} j & 2 & j' \\ -m & -\mu & m' \end{pmatrix}^2 |J_{2\mu}|^2 ,$$

where Q is the factor to be determined by scaling on the single quantum calculation point, and

$$J_{2\mu} = \int_{-\infty}^{+\infty} \frac{1}{r_p^3} Y_\mu^{21}(\hat{r}_p) e^{i\omega_{\alpha\alpha'}t} dt \tag{7}$$

so that

$$\begin{cases} J_{20} = -\sqrt{\frac{5}{4\pi}\frac{1}{v\rho^2}}\beta^2 K_0(\beta) \\ J_{2\pm1} = \mp\frac{2}{3}i\sqrt{\frac{15}{8\pi}\frac{1}{v\rho^2}}\beta^2 K_1(\beta) \\ J_{2\pm2} = \frac{2}{3}\sqrt{\frac{15}{32\pi}\frac{1}{v\rho^2}}\beta^2 [K_0(\beta) + \frac{2}{\beta}K_1(\beta)] \end{cases} \tag{8}$$

where

$$\beta = \frac{\omega_{\alpha\alpha'}\rho}{v} \tag{9}$$

and $K_{0,1}$ are the modified Bessel functions of order 0,1. The total probability (summed and/or averaged over the magnetic quantum numbers) is in agreement with the calculation of Stauffer and McDowell (1965, 1966).

The transition cross-section is obtained by integration over the impact parameter

$$\sigma(\mathbf{v}) = \int_0^\infty P_{\alpha\alpha'}(\rho, \mathbf{v})\, 2\pi\rho\, d\rho . \tag{10}$$

In the case of permitted lines, a cut-off radius ρ_0 must be introduced because at small ρ, $P_{\alpha\alpha'}(\rho, \mathbf{v})$ may become larger than unity and thus unphysical. The cut-off is performed at ρ_0 given by $P_{\alpha\alpha'}(\rho_0, \mathbf{v}) = 1/2$ if this ρ_0 is larger than the largest of the two atomic radii for the two states α and α'. Refined values of the probability at the cut-off, based on degeneracy considerations in the case of multiplets, were proposed in the literature (Seaton, 1964; Bernstein et al., 1963; Sahal-Bréchot, 1974). But in the case of a forbidden line $P_{\alpha\alpha'}(\rho, \mathbf{v})$ remains largely smaller than unity, and we evaluated the atomic radius ρ_0 value from the single quantum calculated point.

$$\sigma(\mathbf{v}) = P_{\alpha\alpha'}(\rho_0, \mathbf{v})\pi\rho_0^2 + \int_{\rho_0}^\infty P_{\alpha\alpha'}(\rho, \mathbf{v})\, 2\pi\rho\, d\rho , \tag{11}$$

leading to

$$\begin{aligned} \sigma_\mu(\mathbf{v}) = {} & P_{\alpha\alpha'}(\rho_0, \mathbf{v})\pi\rho_0^2 \\ & + \pi a_0^2 Z_p^2 \left(\frac{\Delta E_{jj'}}{E}\right)^2 \left(\frac{m_p}{m_e}\right)^2 Q(2j+1) \\ & \times \begin{pmatrix} j & 2 & j' \\ -m & -\mu & m' \end{pmatrix}^2 W_\mu A_\mu , \end{aligned} \tag{12}$$

where

$$E = \frac{1}{2} m_p v^2 \tag{13}$$

is the energy of the incident perturber, and

$$\begin{cases} A_0 = \frac{1}{4}\beta_0^2 [K_1^2(\beta_0) - K_0^2(\beta_0)] \\ A_{\pm1} = \frac{1}{3}[\beta_0 K_1(\beta_0) K_0(\beta_0) \\ \qquad - \frac{1}{2}\beta_0^2 [K_1^2(\beta_0) - K_0^2(\beta_0)]] \\ A_{\pm2} = \frac{1}{12}[2K_1^2(\beta_0) \\ \qquad + \frac{1}{2}\beta_0^2 [K_1^2(\beta_0) - K_0^2(\beta_0)]] \end{cases} . \tag{14}$$

As in Bommier (2006), the momentum transfer during the collision is taken into account via the W_μ factor

$$\begin{cases} W_0 = 1 \\ W_{\pm1} = W_{\pm2} = 1 - \sqrt{\frac{\Delta E_{jj'}}{E}} \end{cases} . \tag{15}$$

This factor is based on classical arguments like those introduced by Duncan (1959), to restrict the transition to the $\Delta m = 0$ components at threshold, following also Percival and Seaton (1958), and to progressively allow the $\Delta m \neq 0$ others when increasing the energy. The factor itself was built on solid angle considerations about the angular momentum transfer. The question in the present work was to extend the factor to the $\Delta m = \pm 2$ case that appears in the quadrupolar interaction. We decided to treat in the same way all the $\Delta m \neq 0$ transitions, whatever the exact Δm value is.

The polarization was then computed by using the irreducible tensors formalism as introduced in Sahal-Bréchot (1977). The cross-section for transition from the k-th order of the j level to the k'-th order of the j' level is then

$$\begin{aligned} Q(jk \to j'k') = {} & \pi a_0^2 Z_p^2 \left(\frac{\Delta E_{jj'}}{E}\right)^2 \left(\frac{m_p}{m_e}\right)^2 Q \\ & \times (2j+1)\sqrt{(2k+1)(2k'+1)} \\ & \times \sum_K (2K+1) \begin{pmatrix} k & k' & K \\ 0 & 0 & 0 \end{pmatrix} \begin{Bmatrix} j & j & k \\ j' & j' & k' \\ 2 & 2 & K \end{Bmatrix} \\ & \times \sum_\mu (-1)^{k+\mu} \begin{pmatrix} 2 & 2 & K \\ \mu & -\mu & 0 \end{pmatrix} W_\mu A_\mu , \end{aligned} \tag{16}$$

which leads to the particular result

$$\begin{aligned} Q(j0 \to j'2) = {} & \pi a_0^2 Z_p^2 \left(\frac{\Delta E_{jj'}}{E}\right)^2 \left(\frac{m_p}{m_e}\right)^2 Q \\ & \times (-1)^{j+j'} \sqrt{5(2j+1)} \begin{Bmatrix} 2 & 2 & 2 \\ j' & j' & j \end{Bmatrix} \\ & \sum_\mu (-1)^\mu \begin{pmatrix} 2 & 2 & 2 \\ \mu & -\mu & 0 \end{pmatrix} W_\mu A_\mu \end{aligned} \tag{17}$$

for the alignment creation in the upper level. Analogous expressions were used for the transition rate. The polarization

Calculation (Bommier et al. 2011)

is finally computed following Eqs. (4) and (14) of Sahal-Bréchot (1977), but with $\epsilon = -1$ here because of the dipolar magnetic emission (as in Sahal-Bréchot, 1974, Eq. 26).

$$\tau = \epsilon \frac{3\eta \sin^2\theta}{1 + (3\cos^2\theta - 1)\eta},$$

$$\eta = \frac{1}{2\sqrt{2}} \frac{\begin{Bmatrix} J & J & 2 \\ 1 & 1 & J' \end{Bmatrix}}{\begin{Bmatrix} J & J & 0 \\ 1 & 1 & J' \end{Bmatrix}} \frac{{}^{JJ}\rho_0^2}{{}^{JJ}\rho_0^0},$$

where the symbols inside braces { } are "6*j*" coefficients.

${}^{JJ}\rho^2$ is the alignement.

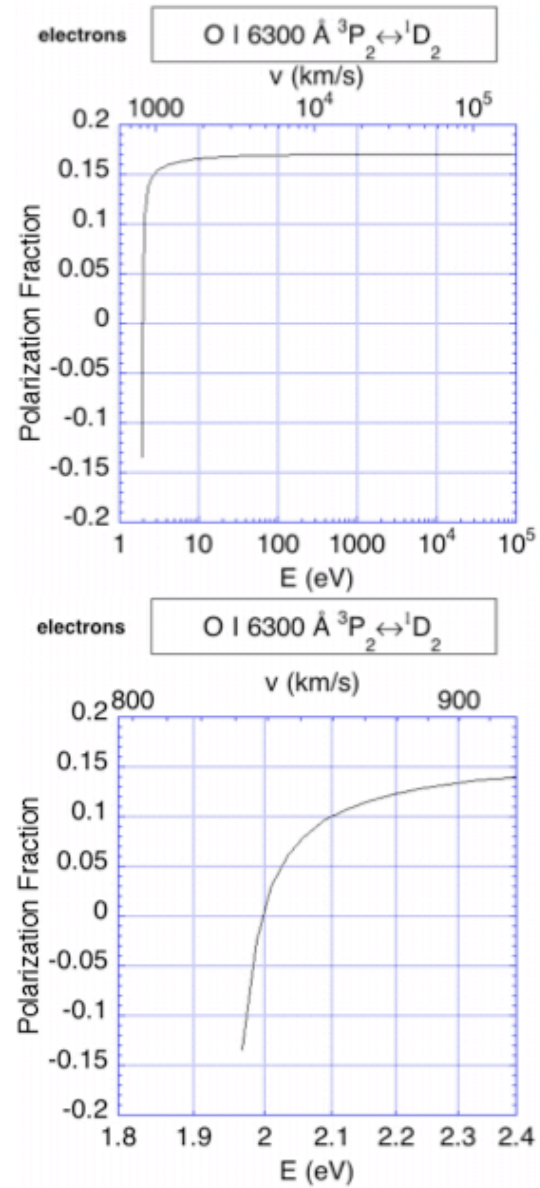

Fig. 2. Impact polarization (linear polarization) due to line collisional excitation by directive electrons, as a function of the energy of the colliding electron, which is assumed to propagate along O_x, the radiation being observed along O_z. A positive polarization means *radial* polarization, i.e. oriented also along O_x, lying inside the scattering plane. A negative polarization means *tangential* polarization, i.e. oriented along O_y, perpendicular to the scattering plane. Bottom: zooming in around the threshold energy, 1.967 eV.

calculation (following…)

- Depolarisation processes
  - Calculation of the density matrix in the thermodynamical conditions
  - Pb of the angular distribution function during the collision processes.
  - …

What kind of information:

- Energy of the precipitating particles?
- Portion of secondary electrons
- particles concentration?
- Angular distribution function?

Or a mix of these?

Polarisation of Jovian Aurora

(Barthelemy et al 2011)

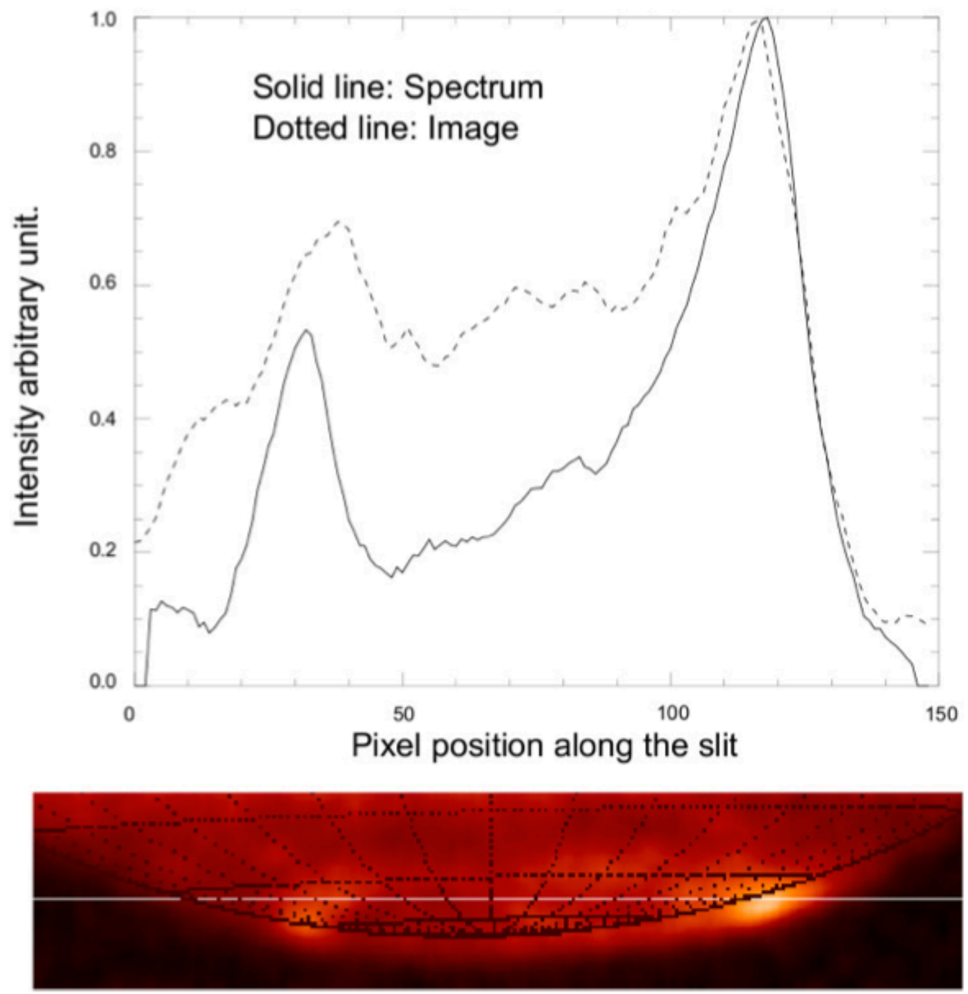

Fig. 2. Position of the slit on the planet, determined from matching the intensity profile of the 3.953 μm line to a cut of the brightness of the Brackett α image. UT 0721, CML 53.51.

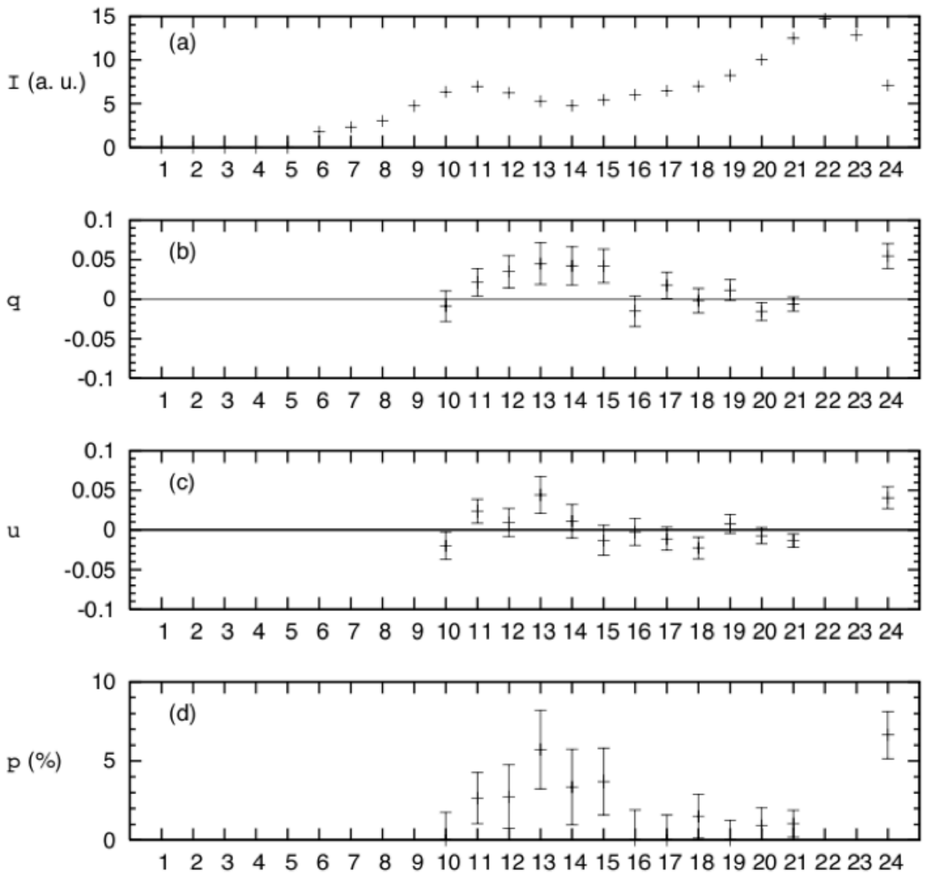

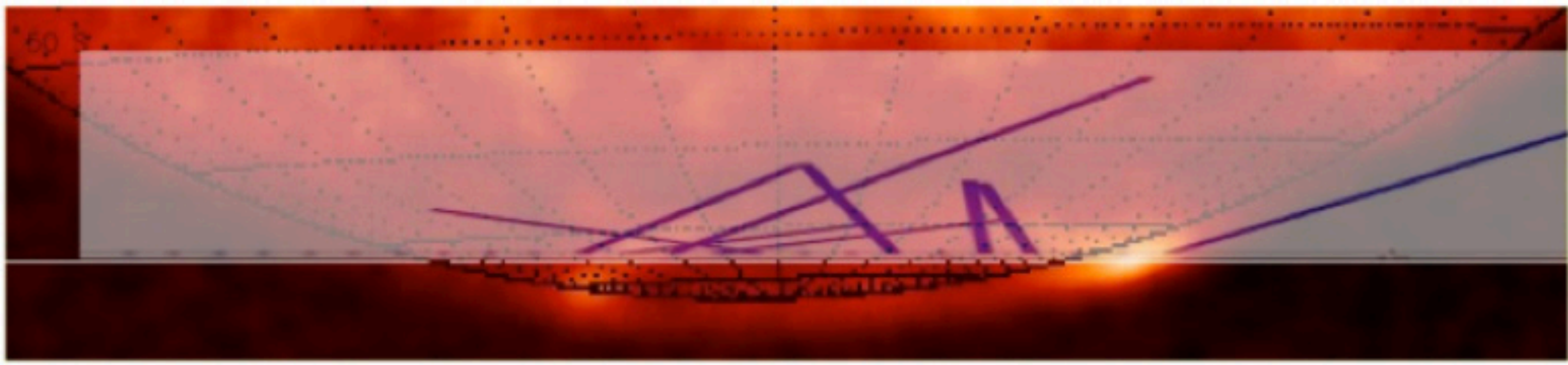

Fig. 8. Polarisation direction for data set 8, overlayed on the disk recorded at 7:49 UT. The length of the vector represents the polarisation degree.

Annexe

- Futur atmospheric polarisation measurements:
  - Lightning/sprites
    - » Strong discharges. Asymetry source : Electric Field.
    - » Pb : very few theoritical calculation on this point

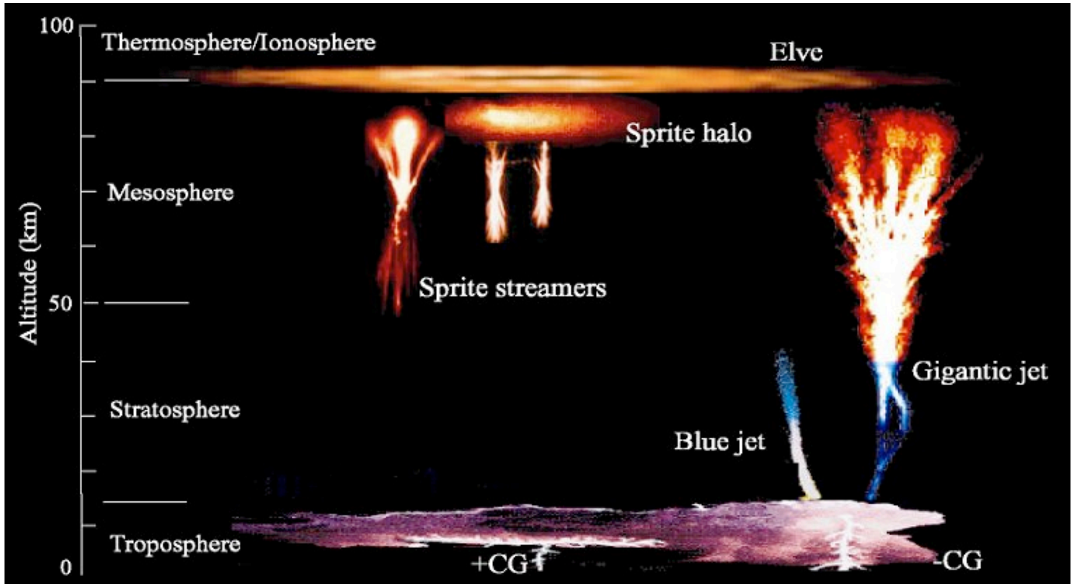

From CNES Taranis team.